



## Lattice Polarisation Effects in the Bandstructure of Semiconductors

Written by:

Matthew Helmi Leth Larsen (s173078)

Supervised by:

Prof. Kristian Sommer Thygesen & Morten Niklas Gjerding

Kongens Lyngby 2019

**DTU Physics**  
**Centre of Atomic Scale Materials Design**  
**Technical University of Denmark**

Fysikvej  
Building 307  
2800 Kongens Lyngby, Denmark  
info@fysik.dtu.dk  
Tel.: +45 4525 3344  
Fax: +45 4593 2399

# Abstract

Lattice contributions to the screened Coulomb interaction ( $W$ ) of the GW formalism are implemented via the dielectric function. An expression for the lattice susceptibility is derived involving the effective Born-charge. Upon inclusion of the lattice susceptibility to the total dielectric function, the conventional electronic contribution is separated from the lattice contribution. The self-energy containing the lattice contribution is solved by a contour integral, thus capturing the dynamics of the lattice effects. A close analysis is presented for the volume confinement of  $W$  in  $\mathbf{q}$ -space, by deriving appropriate expressions in the limits of  $\mathbf{q} \rightarrow 0$  and finite- $\mathbf{q}$ .

The lattice corrections to GW quasi-particle eigen-energies are evaluated numerically by constructing an Atomic Simulation Recipe (ASR) Python module within GPAW. It is emphasised that singularities arise that require special treatment. An analysis of the point-summation in  $\mathbf{q}$ -space present solutions in a high  $\mathbf{k}$ -point density, tuning of the infinitesimal  $\eta$  parameter, and integrating micro-volumes in the Brillouin-Zone.

An energy mask is constructed to control the volume of  $\mathbf{q}$ -space involved in the evaluation. The constructed ASR Python module is tested on Lithium-Fluoride. A cut-off energy of 2.0 eV is proven sufficient. This analysis also proved that inter-band matrix elements were negligible compared to intra-band matrix elements in the lattice corrections. The evaluation of the resulting band-structures presented a desired decrease in the GW band-gap. The results however also exhibited sporadic variations in the lattice corrections, which are attributed to the singularities occurring in the evaluation. The importance of the  $\mathbf{k}$ -point density,  $\eta$  value, and the effectiveness of the micro-volume integration method are presented and discussed.



# Preface and Declaration

This M.Sc. thesis was prepared at the department of physics at the Technical University of Denmark in fulfilment of the requirements for acquiring a Master of Science in Engineering degree in Physics and Nanotechnology with a specialisation in nano-scale materials physics. The work presented was conducted between February and July 2019, under the supervision of Prof. Kristian Sommer Thygesen and Morten Niklas Gjerding.

I hereby declare that I have produced this work without the prohibited assistance of third parties and without making use of aids other than those specified. This work has not previously been presented in any identical or similar form to any other Danish or foreign examination board.

---

Kongens Lyngby, July 28, 2019  
Matthew Helmi Leth Larsen (s173078)



# Acknowledgements

I would like to thank both Prof. Kristian Sommer Thygesen and Morten Niklas Gjerding for the opportunity to conduct a project on this stimulating topic. Since I embarked on my Master's education it has been my goal to specialise myself in computational atomic-scale materials physics and I have had a specific interest in GW calculations. Alongside this, I find that the Atomic Simulation Recipe (ASR) project is exciting and believe it will provide a great value for future students entering the field as I did. I am therefore grateful for the chance to make a contribution, and for all the supportive discussions I have had with both supervisors.

A special thanks goes to Morten Niklas Gjerding for the countless hours of support with derivations, coding, and proof reading. I am greatly appreciative for the many ideas you have provided and the help you have offered whenever I felt stuck.





*Dedicated to my younger brothers, Jeremy Johan and Benjamin Norman.  
I challenge you both to understand this.*



# Contents

Abstract	i
Preface	iii
Acknowledgements	v
1 Introduction	1
1.1 Theoretical Motivation . . . . .	1
1.2 Thesis Scope and Outline . . . . .	3
2 Density Functional Theory	5
2.1 The Many-Electron Problem . . . . .	5
2.2 Local Density Approximation Functional . . . . .	7
2.3 Perdew-Burke-Ernzerhof Functional . . . . .	7
3 The GW Formalism	9
3.1 The Quasi-Particle Picture . . . . .	9
3.2 The GW Self-Energy . . . . .	10
3.2.1 In the Limit of Vanishing $\mathbf{q}$ . . . . .	11
3.3 The Dielectric Function . . . . .	12
4 Lattice Susceptibility via Born-Charges	13
5 Mathematical Analysis of the Lattice Contribution	17
5.1 Separating the Electronic and Lattice Contribution to the Dielectric Function	17
5.2 Analytic Solution to the Self-Energy . . . . .	18
5.2.1 Revisiting the Vanishing $\mathbf{q}$ Limit . . . . .	21
6 Implementation as an Atomic Simulation Recipe	23
6.1 Prerequisite Variables from Existing Recipes . . . . .	24
6.2 Recipe for GW Corrections from Lattice Contributions . . . . .	24
6.3 Treating Numerical Singularities . . . . .	25
6.3.1 Microvolume Integration . . . . .	25
6.3.2 Tuning the $\eta$ Parameter . . . . .	29
7 Correcting the Bandstructure of Lithium-Fluoride	33
7.1 Constructing the Primitive Unit-Cell . . . . .	33
7.2 Convergence in $\mathbf{q}$ -space . . . . .	34
7.3 Evaluation of the Resulting Bandstructures . . . . .	36
8 Conclusion	45
9 Outlook	47
Bibliography	51



# Introduction

Increased computational power has bridged the gap between theorists and experimentalists, not solely in the field of physics. Simulations provide a seemingly infinite playground, and with the ability to simulate a plethora of properties, theorists now have the ability to guide experimentalists in their mutual quest to realise new phenomena and technologies [1, 2]. Density Functional Theory (DFT) has proven itself to be one of the most popular formalisms and methods in obtaining various properties and calculating the electronic structure of materials [3]. With this said, DFT has its shortcomings. For instance, the Kohn-Sham single-particles are well known to provide an improper description of physical excitation energies and significantly underestimate the quasi-particle energy gaps. DFT is typically improved by tweaking and/or constructing new exchange-correlation potentials by modelling more complex effects [3, 4, 5]. The preferred method, however, to obtain more accurate energy band-structures is via the GW formalism [6, 7, 8].

## 1.1. Theoretical Motivation

Initially proposed by Hedin [9], the GW formalism accounts for the screening of charges in a material, due to the presence of other charges, potentially of opposite sign, which is a many-body effect. GW is derived from many-body perturbation theory where the key quantity is the so-called self-energy,  $\Sigma$ . The self-energy, like the exchange-correlation functional in DFT, embodies all complex behaviour of the system. It is this variable that involves the screening and alterations of particles in a system, which gives rise to the quasi-particle. The GW approximation is a first order approximation to the self-energy expanded in terms of the screened Coulomb potential,  $W$ , which symbolically reads

$$\Sigma = iGW, \quad (1.1)$$

where  $G$  represents a single-particle Green's function.

One of the key variables in obtaining the screened Coulomb potential, in order to evaluate the self-energy, is the dielectric function,  $\varepsilon$ . The dielectric function relates the total field of a material to an external field by

$$U_{\text{tot}} = \varepsilon^{-1}U_{\text{ext}}. \quad (1.2)$$

This describes the response of a material to an applied field and embodies, amongst other things, the screening effects in the material [10]. The dielectric and thus the response of a material is frequency ( $\omega$ ) dependent and exhibits features in different frequency regimes. The two frequency regimes that will be of focus is the regime where electronic transitions occur, which are defined by the electronic band-gap energy,  $E_{\text{gap}}$ , and the regime where lattice contributions occur through intrinsic vibrations known as phonons. The expression

for the dielectric in the latter regime is

$$\varepsilon(\omega) = \varepsilon_\infty - \frac{\omega_0^2}{\omega_0^2 - \omega^2 - i\eta\omega}(\varepsilon_s - \varepsilon_\infty) \quad (1.3)$$

where  $\varepsilon_\infty$  denotes the dielectric constant in-between the two regimes,  $\varepsilon_s$  is the dielectric constant below the lattice regime,  $\omega_0$  is a phonon mode, which in polar crystals can be identified as the transverse-optical (TO) mode,  $\omega_{\text{TO}}$ , and  $\eta$  is an infinitesimal quantity representing frictional losses [10]. The contributions of the two regimes along the frequency axis, and the mentioned quantities are illustrated in figure 1.1. Here it is important to note the difference in order of magnitude between  $\omega_{\text{TO}}$  and  $E_{\text{gap}}$ , where the contributions in the respective regimes occur. Phonon modes occur in the meV range, where as semiconductor/insulator electronic band-gaps occur in the eV range [10]. The contributions are therefore well separated in insulators and many semiconductors, however approach each other as the band-gap reduces.

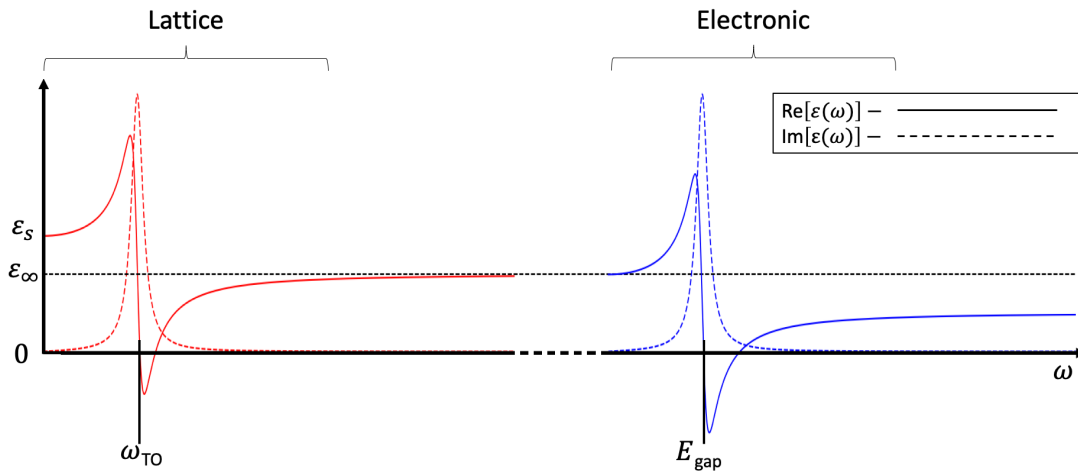


Figure 1.1: Frequency dependence of the Real and Imaginary part of the Dielectric function of a semiconductor/insulator. The lattice contributing and electronic contributing regime are marked and coloured in red and blue, respectively.

GW calculations typically only evaluate the dielectric function in the electronic frequency regime, thus neglecting contributions from the infrared frequency regime that derive from lattice vibrations. It has been shown that GW band-gaps are significantly overestimated for ionic materials [11]. This motivates the inclusion of lattice effects into evaluating the energy band-structure. Including lattice contributions to the GW formalism was originally investigated by Bechstedt *et al.* [12]. They state that the characteristics of polar materials depend strongly on the longitudinal-optical (LO) phonons, which induce large macroscopic electric fields in the material. A strong coupling between these fields and the excited electrons is expected to modify their motion. The coupling between atoms in the lattice and electrons are known as polarons. They hereby pose the question, to what extent the lattice polarisability contributes to the overall screening of electron-hole pairs and the 'dressing' of quasi-particles, i.e. the change in motion and effective mass of a charged particle in the material. They simulate the lattice contribution by adding a lattice polarisability term to the dielectric function. This modifies  $W$ , and was applied only in the static limit ( $\omega = 0$ ) and within the Coulomb-hole static screened exchange (COHSEX) approximation. They show that large corrections are introduced to the band-gap

for strongly ionic materials. Botti and Marques [13] take this a step further and develop a fully *ab-initio* framework to include lattice contributions within the GW scheme and take into account the dynamics in  $W$ . The lattice contribution was mathematically derived starting from the Lyddane-Sachs-Teller relation, which directly involves the longitudinal-transverse optical (LO-TO) phonon splitting into a re-normalisation of the quasi-particle energies. Here it is shown that the lattice contribution decreases the band-gap for a set of binary, polar semiconductors and insulators. With an increase in the size of the LO-TO phonon splitting, the shrinkage of the band-gap also increases, reducing the band-gap percentage error up to a factor of 3. This work is however criticised by Lambrecht *et al.* [14] for improperly treating the volume confinement of  $W$  in  $\mathbf{q}$ -space. They identify the problem of the treatment in the long-wavelength,  $\mathbf{q} \rightarrow 0$ , limit. A solution is proposed by assuming that the lattice contributions are relevant in a finite- $\mathbf{q}$  region defined by an inverse polaron length. They conclude that Botti and Marques over-estimate the correction, however still obtain significant corrections through many methods of implementation.

## 1.2. Thesis Scope and Outline

The focus of this thesis will be to implement lattice contributions through the dielectric function and investigate the effects on the GW band-structures of polar materials. This will be done in a similar manner to Botti and Marques, by deriving an analytic expression for the lattice contribution to the dielectric function. To differentiate from previous works, the derivation will involve the Born-charge and the lattice susceptibility. The Born-charge is a key identifier to the coupling between lattice dynamics and electrostatic fields in a material. A strong emphasis will be placed on the treatment in  $\mathbf{q}$ -space, due to the difficulties highlighted by other works. GW calculations can be made in GPAW, "*a density-functional theory (DFT) Python code based on the projector-augmented wave (PAW) method*" [15, 16]. The analytic expression derived will be implemented into GPAW in order to evaluate the effects numerically. The final aim of the project will be to construct a Python module with the ability to evaluate the dynamic effects of lattice contributions to GW band-structures.

Chapters 2-3 will present the underlying theory of DFT and GW, along with relevant equations. Chapter 4 will discuss the inclusion of lattice effects to the dielectric function via the lattice susceptibility. Chapter 5 will present the derivation of an analytic solution for the lattice contributions to the GW Self-energy, and chapter 6 will describe the implementation of this analytic solution, along with an insight into ensuring a proper numerical treatment. Last but not least, chapter 7 will present the results together with a critical discussion, followed by conclusions and an outlook to further research in chapters 8 and 9, respectively.





## Density Functional Theory

This chapter will provide a brief theoretical overview into Density Functional Theory (DFT) and common Exchange-Correlation functionals, namely the Local Density Approximation (LDA) and Perdew-Burke-Enzerhof (PBE) functional. The theory will be based on Electronic Structure Calculations for Solids and Molecules by Jorge Kohanoff [17].

### 2.1. The Many-Electron Problem

Describing the properties of matter has been a problem that dates back to the very early stages of physics. Matter can be portrayed as a collective interaction between all the atomic constituents. This involves the atomic nuclei and electrons interacting via Coulomb/electrostatic forces. The general Hamiltonian for electrons and nuclei, positioned at  $\mathbf{r}$  and  $\mathbf{R}$ , respectively, can be written as

$$\begin{aligned} \hat{H} = & - \sum_{I=1}^P \frac{\hbar^2}{2M_I} \nabla_I^2 - \sum_{i=1}^N \frac{\hbar^2}{2m} \nabla_i^2 + \frac{e^2}{2} \sum_{I=1}^P \sum_{J \neq I}^P \frac{Z_I Z_J}{|\mathbf{R}_I - \mathbf{R}_J|} \\ & + \frac{e^2}{2} \sum_{i=1}^N \sum_{j \neq i}^N \frac{1}{|\mathbf{r}_i - \mathbf{r}_j|} - e^2 \sum_{I=1}^P \sum_{i=1}^N \frac{Z_I}{|\mathbf{R}_I - \mathbf{r}_i|} \end{aligned} \quad (2.1)$$

in Hartree atomic units, with  $m/e$  as the electron mass/charge and  $M/Z$  as the nuclei mass/charge. This Hamiltonian describes, for  $P$  nuclei and  $N$  electrons, the isolated nucleus and electron kinetic energies, nuclei interactions, electron-electron interactions and nuclei-electron interactions, respectively. With this it is of interest to solve the time-independent Schrödinger equation

$$\hat{H}\Psi(\mathbf{R}, \mathbf{r}) = E\Psi(\mathbf{R}, \mathbf{r}). \quad (2.2)$$

Theoretically, the ability to solve this equation will obtain the ground-state of the system and allow for an accurate calculation of many properties. In practice, the exact solution to this problem is near impossible, as the complexity of the solution increases exponentially with the number of atoms included. This is known as the many-body problem.

To obtain a practical solution approximations are made. Born and Oppenheimer initially proposed the separation of the nuclei motion and electrons. This along with fixing the position of the nucleus, since its relative motion to the electrons in molecules is very small, allowed for a simplification of the many-body problem. This essentially removed the nuclei related terms and parameters in equation (2.1), evolving it into the many-electron problem with the Hamiltonian expressed mathematically as

$$\hat{H}_e = - \sum_{i=1}^N \frac{\hbar^2}{2m} \nabla_i^2 + \frac{e^2}{2} \sum_{i=1}^N \sum_{j \neq i}^N \frac{1}{|\mathbf{r}_i - \mathbf{r}_j|} - e^2 \sum_{I=1}^P \sum_{i=1}^N \frac{Z_I}{|\mathbf{R}_I - \mathbf{r}_i|}, \quad (2.3)$$

where the last term is the Coulomb potential experienced by the electrons, due to the presence of the nuclei. The many-electron problem hereby constitutes a kinetic term, an electron-electron interaction term and an external potential. The many-body electron problem leads to the following ground-state energy by evaluating the many-electron Hamiltonian for the ground-state wave-function.

$$E = T + V_{\text{ext}} + \frac{1}{2} \int \frac{\rho(\mathbf{r})\rho(\mathbf{r}')}{|\mathbf{r} - \mathbf{r}'|} d\mathbf{r}d\mathbf{r}' + E_{\text{XC}}, \quad (2.4)$$

where  $E_{\text{XC}}$  is the exchange and correlation energy. This solution is by definition exact, however the exchange-correlation term is practically determined by approximations. This will be further discussed.

From the work of Hohenberg and Kohn it was observed that the total energy of the many-electron system was strictly a functional of the electron density. This is known as the Hohenberg-Kohn theorem and is embodied by the following rules:

- The external nuclei potential of a system is uniquely determined by the electron density in the ground-state.
- The external potential can determine the many-electron wave-function.
- The total energy of a system is a functional of the many-electron wave-function.

According to this, the result is that the total energy is ultimately a functional of the ground-state electron density. Succeeding this, the Kohn-Sham equations were developed as a way to practically deal with this problem. This involves an expression of the functional, such that the total energy of the ground-state can be written as

$$\begin{aligned} E[\rho] = & -\frac{\hbar^2}{m} \sum_i \int \phi_i^*(\mathbf{r}) \nabla^2 \phi_i(\mathbf{r}) d\mathbf{r} + \int \rho(\mathbf{r}) V_{\text{ext}}(\mathbf{r}) d\mathbf{r} \\ & + \frac{1}{2} \int \int \frac{\rho(\mathbf{r})\rho(\mathbf{r}')}{|\mathbf{r} - \mathbf{r}'|} d\mathbf{r}d\mathbf{r}' + E_{\text{XC}}[\rho] \end{aligned} \quad (2.5)$$

which respectively describes the kinetic energy of  $i$  electrons, the external potential, the Hartree energy and last but not least, the exchange-correlation energy. This divides the functional into terms known exactly from the independent electron approximation and the unknown is covered by the exchange-correlation functional. From the variational principle, the ground-state density is obtainable by minimising the above functional. This in turn means that the exchange-correlation potential is obtainable by minimising the exchange-correlation energy functional. In summary the Kohn-Sham equations are

$$\left[ -\frac{1}{2} \nabla^2 + V_{\text{tot}}(\mathbf{r}) \right] \phi_i = E_i \phi_i(\mathbf{r}), \quad (2.6)$$

$$V_{\text{tot}}(\mathbf{r}) = V_{\text{ext}}(\mathbf{r}) + V_{\text{Hartree}}(\mathbf{r}) + V_{\text{XC}}(\mathbf{r}), \quad (2.7)$$

$$V_{\text{ext}}(\mathbf{r}) = - \sum_I \frac{Z_I}{|\mathbf{r} - \mathbf{R}_I|}, \quad (2.8)$$

$$\nabla^2 V_{\text{Hartree}}(\mathbf{r}) = -4\pi \rho(\mathbf{r}), \quad (2.9)$$

$$V_{\text{XC}}(\mathbf{r}) = \frac{\delta E_{\text{XC}}[\rho]}{\delta \rho}(\mathbf{r}), \text{ and} \quad (2.10)$$

$$\rho(\mathbf{r}) = \sum_i |\phi_i(\mathbf{r})|^2. \quad (2.11)$$

These are solved in a self-consistency loop where an initial electron density is assumed based on an external potential and from this the aim is to loop the equations until the newly obtained electron density reaches self-consistency. The problem in treating the exchange-correlation term remains and will be tackled in the subsequent sections.

## 2.2. Local Density Approximation Functional

The LDA functional has its roots in the study of the homogeneous electron gas. This is similar to the free electron gas problem, however, with an additional component, namely the Coulomb interactions between electrons. In this problem the exchange-correlation is divided linearly as a sum of the exchange term and correlation term. Here the exchange term is available exactly and the correlation term can be determined by numerical methods. Using the homogeneous electron gas intuitively seems wrong, as molecular systems are by no means uniform in their electron densities. The method of the local density approximation treats this issue by considering an in-homogeneous electronic system as locally homogeneous and applies the correlation hole corresponding to the homogeneous electron gas. This in practice means integrating over a certain volume at position,  $\mathbf{r}$ , to obtain the energy based on the electron density assumed at this point. The exchange-correlation functional is expressed as

$$E_{XC}^{LDA}[\rho(\mathbf{r})] = \int \rho(\mathbf{r}) \epsilon_{XC}^{LDA}[\rho(\mathbf{r})] d\mathbf{r}. \quad (2.12)$$

In practice the exchange-correlation energy,  $\epsilon_{XC}^{LDA}$  is calculated by  $\epsilon_X^{LDA} + \epsilon_C^{LDA}$ , where

$$\epsilon_X^{LDA}[\rho(\mathbf{r})] = -\frac{3}{4} \left( \frac{3}{\pi} \right)^{1/3} \rho(\mathbf{r})^{1/3} \quad (2.13)$$

and  $\epsilon_C^{LDA}$  is most accurately obtained by Ceperley *et al.* [18] based on quantum Monte Carlo simulations.

## 2.3. Perdew-Burke-Enzerhof Functional

The LDA functional generally favours more homogeneous systems due to its construction. In order to address the issue of in-homogeneities in the electron density, the gradient of the density is considered. The PBE functional is in the class of Generalised Gradient Approximation (GGA) functionals and handles in-homogeneous systems better than the LDA functional [19]. This is generally expressed as

$$E_{XC}[\rho(\mathbf{r}), \nabla\rho(\mathbf{r}), \nabla^2\rho(\mathbf{r}), \dots] = \int \rho(\mathbf{r}) \cdot \epsilon_{XC}[\rho(\mathbf{r})] \cdot F_{XC}[\rho(\mathbf{r}), \nabla\rho(\mathbf{r}), \nabla^2\rho(\mathbf{r}), \dots] d\mathbf{r} \quad (2.14)$$

which includes higher order derivatives. In the PBE functional the exchange energy can be expressed based on the LDA exchange energy and including an enhancement factor  $F_X$  that depends on the density and the gradient.

$$E_X^{PBE}[\rho(\mathbf{r}), \nabla\rho(\mathbf{r})] = \int \epsilon_X^{LDA}[\rho(\mathbf{r})] \cdot F_X(s) d\mathbf{r} \quad (2.15)$$

where  $s = |\nabla\rho(\mathbf{r})|/(2k_F\rho(\mathbf{r}))$ , is the dimensionless density gradient. Important properties of  $F_X(s)$  are that it satisfies a uniform electron gas limit, so that  $F_X(0) = 1$  and that it satisfies the Local Spin Density Approximation (LSDA) exchange energy limit for  $s \rightarrow 0$ .



## The GW Formalism

The impressive balance between accuracy and computational efficiency of DFT has made it a very popular method in simulating atomic systems, however band-gaps are known to be under-estimated as the Kohn-Sham single-particle energies do not properly describe the quasi-particle energies [6]. This is treated in the GW formalism by introducing the quasi-particle and dynamical screening of the Coulomb interaction. There will be a presentation of the GW method for calculating eigen-energies. This will have a specific focus on a solution to the GW self-energy, alongside describing key concepts entailed in the GW formalism, such as the quasi-particle picture and the screened Coulomb interaction. Methods to treat and solve the GW self-energy will also be described. The equations here will be based on derivations in the work by Hüser *et al.* [7].

### 3.1. The Quasi-Particle Picture

Quasi-particles are introduced in solid-state physics to have a means of better describing the complex behaviour of particle motion in materials. Complex microscopic behaviour of particles in materials alters its properties with respect to a non-interacting particle system. An electron present in a material will undergo a motion affected by other surrounding electrons and nuclei, causing it to behave as an electron with essentially an altered effective mass. This electron can be considered a quasi-particle. The quasi-particle eigen-states are formally defined in terms of the electron creation and annihilation field operators for a spatial point,  $\mathbf{r}$ ,  $\hat{\Psi}^\dagger(\mathbf{r})$  and  $\hat{\Psi}(\mathbf{r})$ , respectively. The definition follows as

$$\psi_{i-}^{*\text{QP}}(\mathbf{r}) = \langle \Psi_i^{N-1} | \hat{\Psi}(\mathbf{r}) | \Psi_0^N \rangle, \quad (3.1)$$

$$\psi_{i+}^{\text{QP}}(\mathbf{r}) = \langle \Psi_i^{N+1} | \hat{\Psi}^\dagger(\mathbf{r}) | \Psi_0^N \rangle, \quad (3.2)$$

where  $|\Psi_i^N\rangle$  denote the many-body eigen-states,  $i$  for an  $N$ -particle system. From this definition, the quasi-particle, strictly speaking, describes an excitation of the many-body system. Similarly, the quasi-particle eigen-energies,  $\varepsilon^{\text{QP}}$ , are understood as excitation energies for  $N \pm 1$  systems from the many-body ground-state eigen-energy,  $E_0^N$  as

$$\varepsilon_{i-}^{\text{QP}} = E_0^N - E_i^{N-1}, \quad (3.3)$$

$$\varepsilon_{i+}^{\text{QP}} = E_i^{N+1} - E_0^N. \quad (3.4)$$

The quasi-particle eigen-states and -energies can be related to a Green's function for a general electron system and must also satisfy the Dyson equation [21]

$$G(\omega) = \sum_i \frac{|\psi_i^{\text{QP}}\rangle \langle \psi_i^{\text{QP}}|}{\omega - \varepsilon_i^{\text{QP}} + i\eta} = [(\omega + i\eta) - H_0 - \Sigma(\omega)]^{-1}. \quad (3.5)$$

Combining the two expressions for the Green's function in equation (3.5), evaluated at  $\omega = \varepsilon_i^{\text{QP}}$  (and  $\eta \rightarrow 0^+$ ), results in the quasi-particle equation,

$$\left[ H_0 + \Sigma(\varepsilon_i^{\text{QP}}) \right] |\psi_i^{\text{QP}}\rangle = \varepsilon_i^{\text{QP}} |\psi_i^{\text{QP}}\rangle, \quad (3.6)$$

which can be solved with a given self-energy. The quasi-particle energies for this evaluation are however unknown and so in practice a starting point is set in a non-interacting system, often using the Kohn-Sham Hamiltonian. This follows equation (2.6), which in an alternate notation reads

$$\left[ H_0 - V^{\text{KS}} \right] |\phi_i^{\text{KS}}\rangle = \varepsilon_i^{\text{KS}} |\phi_i^{\text{KS}}\rangle. \quad (3.7)$$

In applying first-order perturbation theory to the quasi-particle energy and approximating the self-energy, evaluated for the quasi-particle eigen-energy, as a linear expansion results in an expression for the quasi-particle energy that reads

$$\varepsilon_i^{\text{QP}} = \varepsilon_i^{\text{KS}} + Z_i^{\text{KS}} \cdot \langle \phi_i^{\text{KS}} | \Sigma(\varepsilon_i^{\text{KS}}) - V^{\text{KS}} | \phi_i^{\text{KS}} \rangle, \quad (3.8)$$

where

$$Z_i^{\text{KS}} = \left( \langle \phi_i^{\text{KS}} | 1 - \frac{\partial \hat{\Sigma}}{\partial \varepsilon} \bigg|_{\varepsilon_i^{\text{KS}}} | \phi_i^{\text{KS}} \rangle \right)^{-1} \quad (3.9)$$

determines the re-normalisation of the Kohn-Sham energies to the quasi-particle energies. It is clear here that the quasi-particle eigen-energy is a correction to the Kohn-Sham eigen-energy. GW calculations therefore start with a DFT calculation typically using an LDA or GGA functional to obtain the Kohn-Sham eigen-states and -energies, and what remains is to evaluate the self-energy, which theoretically contains effects from all complex behaviour.

### 3.2. The GW Self-Energy

The GW formalism takes its name from the approximation made to the self-energy by Hedin [9]. In his work the self-energy is expanded in terms of the screened Coulomb potential,

$$W(\mathbf{q}, \omega) = \varepsilon^{-1}(\mathbf{q}, \omega) v(\mathbf{q}), \quad (3.10)$$

as opposed to the bare Coulomb potential,  $v(\mathbf{q})$ , dependent on reciprocal  $\mathbf{q}$ -space and frequency,  $\omega$ . The dielectric of the material  $\varepsilon(\mathbf{q}, \omega)$  is an essential tool in describing screening effects of a material and will be further discussed in upcoming sections. The inclusion of the screened Coulomb interaction accounts for both exchange and correlation effects, where the exchange part comes from the Hartree-Fock approximation [10]. The first order term of the expansion in real space and time presents a product between the Green's function and the screened Coulomb interaction. In the frequency domain, this product becomes a convolution [20] that reads

$$\Sigma(\mathbf{r}, \mathbf{r}'; \omega) = \frac{i}{2\pi} \int d\omega' e^{i\eta\omega'} G(\mathbf{r}, \mathbf{r}'; \omega + \omega') W(\mathbf{r}, \mathbf{r}'; \omega'). \quad (3.11)$$

This self energy will be evaluated by Kohn-Sham wavefunctions  $|\phi_{n\mathbf{k}}^{\text{KS}}\rangle$ , where  $n$  and  $\mathbf{k}$  denote the band and  $\mathbf{k}$ -point index. The corresponding Kohn-Sham eigen-values are denoted

by  $\varepsilon_{n\mathbf{k}}^{\text{KS}}$ . This allows for a single-shot calculation of  $G$  and  $W$ , known as the  $G_0W_0$  method, rather than solving Hedin's equations self-consistently. The quasi-particle equation (3.8) in this basis reads

$$\varepsilon_{n\mathbf{k}}^{\text{QP}} = \varepsilon_{n\mathbf{k}}^{\text{KS}} + Z_{n\mathbf{k}}^{\text{KS}} \cdot \langle \phi_{n\mathbf{k}}^{\text{KS}} | \Sigma(\varepsilon_{n\mathbf{k}}^{\text{KS}}) - V^{\text{KS}} | \phi_{n\mathbf{k}}^{\text{KS}} \rangle. \quad (3.12)$$

Taking equation (3.11) and inserting the spectral representation for the Green's function in the described basis and performing a Fourier transform on the screened Coulomb potential to express it in terms of reciprocal space vectors  $\mathbf{q}$  as [21]

$$G(\mathbf{r}, \mathbf{r}'; \omega + \omega') = \sum_{m, \mathbf{k}'} \frac{|\phi_{m\mathbf{k}'}^{\text{KS}}\rangle \langle \phi_{m\mathbf{k}'}^{\text{KS}}|}{\omega + \omega' - \varepsilon_{m\mathbf{k}'}^{\text{KS}} + i\eta \text{sgn}(\varepsilon_{m\mathbf{k}'}^{\text{KS}} - \mu)}, \quad (3.13)$$

$$W(\mathbf{r}, \mathbf{r}'; \omega') = \frac{1}{(2\pi)^6} \int d\mathbf{q} \int d\mathbf{q}' e^{i\mathbf{q}\cdot\mathbf{r}} e^{i\mathbf{q}'\cdot\mathbf{r}'} W(\mathbf{q}, \mathbf{q}'; \omega'), \quad (3.14)$$

with  $\mu$  as the chemical potential, gives the following when evaluating the diagonal matrix elements in band,  $n$  and reciprocal space point,  $\mathbf{k}$ .

$$\begin{aligned} & \langle \phi_{n\mathbf{k}}^{\text{KS}} | \Sigma(\mathbf{q}; \omega) | \phi_{n\mathbf{k}}^{\text{KS}} \rangle \\ &= \frac{1}{\Omega} \sum_{\mathbf{G}, \mathbf{G}'} \sum_{\mathbf{q}}^{\text{B.Z.}} \sum_m \frac{i}{2\pi} \int_{-\infty}^{\infty} d\omega' \frac{\rho_{m\mathbf{k}-\mathbf{q}}^{n\mathbf{k}}(\mathbf{q} + \mathbf{G}) \rho_{m\mathbf{k}-\mathbf{q}}^{*n\mathbf{k}}(\mathbf{q} + \mathbf{G}')}{\omega + \omega' - \varepsilon_{m\mathbf{k}-\mathbf{q}}^{\text{KS}} + i\eta \text{sgn}(\varepsilon_{m\mathbf{k}-\mathbf{q}}^{\text{KS}} - \mu)} W(\mathbf{q} + \mathbf{G}, \omega'), \end{aligned} \quad (3.15)$$

where  $\mathbf{q}$  cover the  $\mathbf{k} - \mathbf{k}'$  transitions within the Brillouin-Zone (B.Z.),  $\Omega$  is the total crystal volume (the unit cell volume times the number of  $\mathbf{k}$ -points:  $\Omega_{\text{cell}} \cdot N_k$ ), and  $\mathbf{G}$  is a reciprocal lattice translation. The pair-densities are defined as

$$\rho_{m\mathbf{k}-\mathbf{q}}^{n\mathbf{k}}(\mathbf{q} + \mathbf{G}) = \langle \phi_{n\mathbf{k}}^{\text{KS}} | e^{i(\mathbf{q}+\mathbf{G})\cdot\mathbf{r}} | \phi_{m\mathbf{k}-\mathbf{q}}^{\text{KS}} \rangle \quad (3.16)$$

and as highlighted by Yan *et al.* [22] a separate treatment is required in the optical/long-wavelength limit due to the divergence of the screened Coulomb potential

$$W(\mathbf{q} + \mathbf{G}, \omega') = \varepsilon^{-1}(\mathbf{q}, \omega') \frac{4\pi}{|\mathbf{q} + \mathbf{G}|^2}, \quad (3.17)$$

when  $\mathbf{G} = 0$  and  $\mathbf{q} \rightarrow 0$ .

### 3.2.1. In the Limit of Vanishing $\mathbf{q}$

In the limit of  $\mathbf{q} \rightarrow 0$ , it will be necessary to force the expression in equation (3.15) to vanish, in order to avoid the divergence. Expressing the pair-densities in terms of Bloch states results in

$$\rho_{m\mathbf{k}-\mathbf{q}}^{n\mathbf{k}}(\mathbf{q}) = \langle u_{n\mathbf{k}} | e^{-i\mathbf{k}\cdot\mathbf{r}} e^{i\mathbf{q}\cdot\mathbf{r}} e^{i(\mathbf{k}-\mathbf{q})\cdot\mathbf{r}} | u_{m\mathbf{k}-\mathbf{q}} \rangle \quad (3.18)$$

$$= \langle u_{n\mathbf{k}} | u_{m\mathbf{k}-\mathbf{q}} \rangle. \quad (3.19)$$

Applying the Hamiltonian [10]

$$H(\mathbf{k}) = -\frac{1}{2}(\nabla + i\mathbf{k})^2 + V(\mathbf{r}) \quad (3.20)$$

and utilising second order perturbation theory on  $|u_{m\mathbf{k}-\mathbf{q}}\rangle$  with a perturbation term  $\tilde{V} = H(\mathbf{k}) - H(\mathbf{k} - \mathbf{q})$  results in an expression for the pair-density in the  $\mathbf{q} \rightarrow 0$  limit, which

reads

$$\rho_{m\mathbf{k}-\mathbf{q}}^{n\mathbf{k}}(\mathbf{q}) = \delta_{nm} - i\mathbf{q} \cdot \frac{\langle u_{n\mathbf{k}} | (\nabla + i\mathbf{k}) | u_{m\mathbf{k}} \rangle}{\varepsilon_{m\mathbf{k}} - \varepsilon_{n\mathbf{k}}}. \quad (3.21)$$

This expression ensures that equation (3.15) is well behaved in the long-wavelength limit. What remains is the evaluation of the screened Coulomb interaction via the dielectric function.

### 3.3. The Dielectric Function

The dielectric function is a fundamental component in describing material properties. It provides the response of a material to an applied external field. It is thus apparent that the dielectric function will contain information about the material's ability to screen its charges. Within the Random Phase Approximation [22], where exchange and correlation effects are ignored, the non-interacting response function,  $\chi^0$ , reads

$$\chi_{\mathbf{G}\mathbf{G}'}^0(\mathbf{q}, \omega) = \frac{1}{\Omega} \sum_{n,m} \sum_{\mathbf{k}} (f_{n\mathbf{k}} - f_{m\mathbf{k}-\mathbf{q}}) \frac{\rho_{m\mathbf{k}-\mathbf{q}}^{n\mathbf{k}}(\mathbf{q} + \mathbf{G}) \rho_{m\mathbf{k}-\mathbf{q}}^{*\mathbf{k}}(\mathbf{q} + \mathbf{G}')}{\omega + \varepsilon_{n\mathbf{k}}^{\text{KS}} - \varepsilon_{m\mathbf{k}-\mathbf{q}}^{\text{KS}} + i\eta}, \quad (3.22)$$

where  $f_{n\mathbf{k}}$  represents the Kohn-Sham occupation for band  $n$  and  $\mathbf{k}$ -point. This is related to the dielectric function as

$$\varepsilon_{\mathbf{G}\mathbf{G}'}(\mathbf{q}, \omega) = \delta_{\mathbf{G}\mathbf{G}'} - \frac{4\pi}{|\mathbf{q} + \mathbf{G}|^2} \chi_{\mathbf{G}\mathbf{G}'}^0(\mathbf{q}, \omega), \quad (3.23)$$

where the off-diagonal terms provide information of the response at reciprocal wave-vectors different to that of the incoming field, relating to a phenomenon known as local-field effects, hence proving the practicality of  $\mathbf{G}\mathbf{G}'$  notation. In practice, the frequency dependence of the dielectric function is treated in the plasmon-pole approximation. In this approximation, the frequency dependence of  $\varepsilon_{\mathbf{G}\mathbf{G}'}^{-1}(\mathbf{q}, \omega)$  is approximated to consist of a single-pole following [13]

$$\varepsilon_{\mathbf{G}\mathbf{G}'}^{-1}(\mathbf{q}, \omega) = \delta_{\mathbf{G}\mathbf{G}'} + \frac{\Omega_{\mathbf{G}\mathbf{G}'}^2(\mathbf{q})}{\omega^2 - [\tilde{\omega}_{\mathbf{G}\mathbf{G}'}(\mathbf{q}) - i\eta]^2}, \quad (3.24)$$

where the two parameters  $\Omega_{\mathbf{G}\mathbf{G}'}^2(\mathbf{q})$  and  $\tilde{\omega}_{\mathbf{G}\mathbf{G}'}(\mathbf{q})$  are fitted by evaluating  $\varepsilon_{\mathbf{G}\mathbf{G}'}^{-1}(\mathbf{q}, \omega)$  at  $\omega = 0$  and  $\omega = i\omega_p$ , and  $\omega_p$  is the plasmon frequency. This is currently how the dielectric function is evaluated for the electronic frequency regime highlighted in figure 1.1. This project sets out to determine the dielectric in the infrared frequency regime, where lattice contributions occur, and include this into the GW formalism.



## Lattice Susceptibility via Born-Charges

The aim of the following will be to present how intrinsic lattice effects can be implemented into the dielectric function by using the lattice susceptibility expressed in terms of the Born-charges. Consider a general 3-Dimensional crystal, where  $a$  labels the atoms, and  $\nu$  a Cartesian direction. A displacement of an atom is contained in the vector  $\mathbf{U}$  with components  $u_\nu^a$ . The ground state energy expanded to the second order within the harmonic approximation reads

$$E_0(\mathbf{U}) = E_0(0) + \frac{1}{2} \sum_{a\nu, a'\nu'} \left( \frac{\partial^2 E_0}{\partial u_\nu^a \partial u_{\nu'}^{a'}} \right)_0 u_\nu^a u_{\nu'}^{a'}, \quad (4.1)$$

where  $a, a' = 1, 2, \dots, A$ ;  $\nu, \nu' = x, y, z$ ; and  $( )_0$  denotes that the derivative is evaluated at the equilibrium position, hence the disappearance of the first-order derivative [10]. The force constant matrix, containing the forces exerted in Cartesian directions on each atom due to the displacement of another atom in a Cartesian direction, is defined as

$$C_{\nu\nu'}^{aa'} = \left( \frac{\partial^2 E_0}{\partial u_\nu^a \partial u_{\nu'}^{a'}} \right)_0. \quad (4.2)$$

For a polar material this energy can be perturbed by the energy of a dipole,  $\mathbf{p}$ , in an electric field,  $\mathbf{E}$ . This gives

$$E_{\text{dipole}} = -\mathbf{p} \cdot \mathbf{E} = -\Omega_{\text{cell}} \mathbf{P} \cdot \mathbf{E}, \quad (4.3)$$

where the final equality introduces the polarisation density,  $\mathbf{P}$ , defined as the dipole moment per unit-cell volume,  $\Omega_{\text{cell}}$  [23]. Superposing equations (4.1) and (4.3) in vector notation, and regarding  $E_0(0)$  as a reference energy provides an energy functional, expressing the total energy of a system.

$$\Phi = \frac{1}{2} \mathbf{U}^\dagger \cdot \mathbf{C} \cdot \mathbf{U} - \Omega_{\text{cell}} \mathbf{P} \cdot \mathbf{E}, \quad (4.4)$$

where, as mentioned,  $\mathbf{U}$  represent the displacements of the system,  $\mathbf{C}$  is the force constant matrix,  $\mathbf{E}$  is the electric field, and  $\mathbf{P}$  the corresponding polarisation density. The polarisation density can then be expanded in terms of the displacement and electric field to the first order as

$$\mathbf{P}(\mathbf{E}, \mathbf{U}) = \mathbf{P}_0 + \left. \frac{\partial \mathbf{P}}{\partial \mathbf{U}} \right|_{E=0} \cdot \mathbf{U} + \left. \frac{\partial \mathbf{P}}{\partial \mathbf{E}} \right|_{U=0} \cdot \mathbf{E} = \frac{|e|}{\Omega_{\text{cell}}} \mathbf{Z} \cdot \mathbf{U} + \varepsilon_0 \chi_e \cdot \mathbf{E}. \quad (4.5)$$

To explain the final equality, for a non-ferroelectric material the zero'th order term vanishes (i.e.  $\mathbf{P}_0 = 0$ ) and the expressions for the derivatives are by definition

$$\left. \frac{\partial \mathbf{P}}{\partial \mathbf{U}} \right|_{E=0} = \frac{|e|}{\Omega_{\text{cell}}} \mathbf{Z} \quad \text{and} \quad \left. \frac{\partial \mathbf{P}}{\partial \mathbf{E}} \right|_{U=0} = \varepsilon_0 \boldsymbol{\chi}_e, \quad (4.6)$$

where  $\mathbf{Z}$  represents the atomic Born-charges,  $\boldsymbol{\chi}_e$  is the electronic susceptibility, and  $\varepsilon_0$  is the vacuum permittivity [23, 24].

The Born-charge entails the coupling between lattice dynamics and electrostatic fields, which makes it a proper candidate in describing the lattice susceptibility of a material. The definition of the Born-charge is presented as the change in the polarisation density divided by the amount that an atom is displaced. The expansion in equation (4.5) introduces a dot product between the Born-charges and the displacements, which is clarified below.

$$\mathbf{Z} \cdot \mathbf{U} = \sum_{a,\nu} z_{\nu\nu'}^a u_{\nu'}^a, \quad (4.7)$$

which reveals the Born-charges as a tensor, implying that by displacing an atom in one Cartesian direction, can induce a change in polarisation density in that direction, but can also induce a change in polarisation density in another Cartesian direction. The  $a$  and  $\nu'$  indices are collapsed into a shared index, so the dot product for two atoms looks like

$$\mathbf{Z} \cdot \mathbf{U} = \begin{matrix} \nu=x \\ \nu=y \\ \nu=z \end{matrix} \begin{bmatrix} z_x^1 & z_y^1 & z_z^1 & z_x^2 & z_y^2 & z_z^2 \\ z_x^1 & z_y^1 & z_z^1 & z_x^2 & z_y^2 & z_z^2 \\ z_x^1 & z_y^1 & z_z^1 & z_x^2 & z_y^2 & z_z^2 \end{bmatrix} \cdot \begin{bmatrix} u_x^1 \\ u_y^1 \\ u_z^1 \\ u_x^2 \\ u_y^2 \\ u_z^2 \end{bmatrix}, \quad (4.8)$$

which results in a vector in which the dimensions are the Cartesian directions of the induced changes in polarisation density.

A relation between  $\mathbf{E}$  and  $\mathbf{U}$  is derived by the equation of motion which reads

$$\mathbf{M} \frac{\partial^2 \mathbf{U}}{\partial t^2} = -\frac{\partial \Phi}{\partial \mathbf{U}} = -\mathbf{C} \cdot \mathbf{U} + |e| \mathbf{Z}^T \cdot \mathbf{E}, \quad (4.9)$$

The matrix,  $\mathbf{M}$ , contains the mass of each atom and is diagonal. For two atoms this looks like

$$\mathbf{M} = \begin{matrix} & \begin{matrix} x & y & z \end{matrix} \\ \begin{matrix} x \\ y \\ z \end{matrix} & \begin{bmatrix} M_1 & 0 & 0 \\ 0 & M_1 & 0 \\ 0 & 0 & M_1 \end{bmatrix} \end{matrix} \quad (4.10)$$

and thus the matrix elements are denoted  $M_a$ . The equation of motion can be re-arranged for  $\mathbf{U}$ , using  $\partial^2 \mathbf{U} / \partial t^2 = -\omega^2 \mathbf{U}$  for a harmonic displacement with a vibrational mode,  $\omega$

resulting in,

$$\mathbf{U} = |e| \left( \mathbf{C} - \mathbf{M}\omega^2 \right)^{-1} \cdot \mathbf{Z}^T \cdot \mathbf{E}. \quad (4.11)$$

By substituting this expression into equation (4.5) for the polarisation density, the lattice susceptibility can now be deduced by the definition of the electric displacement field [23]

$$\mathbf{D} \equiv \varepsilon_0 \mathbf{E} + \mathbf{P} \quad (4.12)$$

$$= \varepsilon_0 \mathbf{E} + \frac{|e|^2}{\Omega} \mathbf{Z} \cdot \left( \mathbf{C} - \mathbf{M}\omega^2 \right)^{-1} \cdot \mathbf{Z}^T \cdot \mathbf{E} + \varepsilon_0 \boldsymbol{\chi}_e \cdot \mathbf{E} \quad (4.13)$$

$$= \varepsilon_0 (1 + \boldsymbol{\chi}_{\text{lat}} + \boldsymbol{\chi}_e) \cdot \mathbf{E} \quad (4.14)$$

$$= \varepsilon_0 (1 + \boldsymbol{\chi}) \cdot \mathbf{E}, \quad (4.15)$$

where the lattice susceptibility is defined as

$$\boldsymbol{\chi}_{\text{lat}} = \frac{1}{\varepsilon_0} \frac{|e|^2}{\Omega_{\text{cell}}} \mathbf{Z} \cdot \left( \mathbf{C} - \mathbf{M}\omega^2 \right)^{-1} \cdot \mathbf{Z}^T, \quad (4.16)$$

$$= \frac{4\pi}{\Omega_{\text{cell}}} \mathbf{Z} \cdot (\sqrt{\mathbf{M}})^{-1} \cdot \left( \boldsymbol{\mathcal{D}} - \omega^2 \mathbf{I} \right)^{-1} \cdot (\sqrt{\mathbf{M}})^{-1} \cdot \mathbf{Z}^T. \quad (4.17)$$

The final equality is in Gaussian-cgs units and substitutes the dynamical matrix,  $\boldsymbol{\mathcal{D}}$ , related to the force constant matrix as

$$\boldsymbol{\mathcal{D}} = (\sqrt{\mathbf{M}})^{-1} \mathbf{C} (\sqrt{\mathbf{M}})^{-1} \quad \text{or} \quad \mathcal{D}_{\nu\nu'}^{aa'} = C_{\nu\nu'}^{aa'} \frac{1}{\sqrt{M_a M_{a'}}} \quad (4.18)$$

which contains the phonon frequencies,  $\omega$ , and displacements,  $\mathbf{u}$ , for each mode,  $i$ , as eigen-values and -vectors, respectively. The expression can be reformed to an expansion over the eigen-values/-vectors as

$$\boldsymbol{\chi}_{\text{lat}} = \frac{4\pi}{\Omega_{\text{cell}}} \mathbf{Z} \cdot (\sqrt{\mathbf{M}})^{-1} \cdot \sum_i \frac{\mathbf{u}_i \mathbf{u}_i^T}{(\omega_i + (\omega + i\eta))(\omega_i - (\omega + i\eta))} \cdot (\sqrt{\mathbf{M}})^{-1} \cdot \mathbf{Z}^T. \quad (4.19)$$

The effective Born-charge is defined as

$$\bar{\mathbf{Z}} = \mathbf{Z} \cdot (\sqrt{\mathbf{M}})^{-1} \cdot \mathbf{u}. \quad (4.20)$$

It can be assumed for polar semiconductors that there is a single dominating mode in the sum, which can be identified as the TO phonon mode (see figure 1.1). This reduces the effective Born-charge to a single mode, corresponding to the TO phonon mode, which simplifies the lattice susceptibility to the following, allowing  $\eta \rightarrow 0$

$$\chi_{\text{lat}} = \frac{4\pi}{\Omega_{\text{cell}}} \frac{1}{(\omega_{\text{TO}}^2 - \omega^2)} \bar{\mathbf{Z}}^2. \quad (4.21)$$

The lattice susceptibility is related to the dielectric function by  $\varepsilon = \varepsilon_e + \chi_{\text{lat}}$ , which is by definition zero when  $\omega = \omega_{\text{LO}}$ , the LO frequency [10]. From this it is seen that the effective Born-charge is related to the LO-TO phonon splitting by

$$\omega_{\text{LO}}^2 - \omega_{\text{TO}}^2 = \frac{4\pi}{\varepsilon_{\infty} \Omega_{\text{cell}}} \bar{\mathbf{Z}}^2, \quad (4.22)$$

where  $\varepsilon_{\infty}$  is the electronic dielectric contribution in the phonon frequency regime (see

figure 1.1). From this relation it is further emphasised how the Born-charge describes the coupling between lattice dynamics and electrostatic fields. Since the LO-TO phonon splitting arises from the long-range Coloumb interactions, the Born-charges are then an indicator of these interactions. This provides a theoretical connection to the work performed by Botti and Marques [13], studying the band-gap re-normalisation of lattice polarisation effects with a direct dependence on the LO-TO splitting.

## Mathematical Analysis of the Lattice Contribution

The following chapter will present a derivation of an analytic solution to the lattice contribution of the self-energy in the GW formalism, described in section 3.2. This will begin with obtaining an expression for a corrective term in the total dielectric function depending on the lattice susceptibility expressed in equation (4.21). Succeeding this, the total dielectric function will be implemented into the GW formalism and a solution will be presented to the corrective term utilising methods of complex analysis.

### 5.1. Separating the Electronic and Lattice Contribution to the Dielectric Function

Calculations involving the electronic component of the dielectric function are well covered and thus the desire is to obtain an expression presenting a corrective term to include in the total dielectric function in addition to the electronic contribution. The dielectric constant can be expressed in terms of the susceptibility as [23]

$$\varepsilon \equiv 1 + \chi. \quad (5.1)$$

The susceptibility,  $\chi$ , contains both the electronic and lattice contribution,  $\chi_e$  and  $\chi_{\text{lat}}$ , respectively. Moving into reciprocal lattice,  $\mathbf{G}$ , space and expressing the dielectric function and susceptibilities as matrices in  $\mathbf{G}\mathbf{G}'$  with dependencies on the reciprocal Brillouin-Zone vectors,  $\mathbf{q}$ , and frequency,  $\omega$ , reads

$$\varepsilon_{\mathbf{G}\mathbf{G}'}(\mathbf{q}, \omega) = 1 + \left( \chi_{e,\mathbf{G}\mathbf{G}'}(\mathbf{q}, \omega) + \chi_{\text{lat},\mathbf{G}\mathbf{G}'}(\mathbf{q}, \omega) \right) \quad (5.2)$$

$$= \varepsilon_{e,\mathbf{G}\mathbf{G}'}(\mathbf{q}, \omega) + \chi_{\text{lat},\mathbf{G}\mathbf{G}'}(\mathbf{q}, \omega). \quad (5.3)$$

From here on the  $\mathbf{q}$  and  $\omega$  dependencies will be omitted for simpler notation until otherwise specified. Implementing equation (5.3) into the GW formalism will require an inverse of the right hand side, following equations (3.10) and (3.15), which is an inverse of a sum of matrices (i.e.  $(\varepsilon_{e,\mathbf{G}\mathbf{G}'} + \chi_{\text{lat},\mathbf{G}\mathbf{G}'})^{-1}$ ). Following Botti and Marques [13], this inversion can be expressed as

$$\varepsilon_{\mathbf{G}\mathbf{G}'}^{-1} = \varepsilon_{e,\mathbf{G}\mathbf{G}'}^{-1} - \frac{1}{1 + \text{Tr} \left\{ \chi_{\text{lat},\mathbf{G}\mathbf{G}'} \cdot \varepsilon_{e,\mathbf{G}\mathbf{G}'}^{-1} \right\}} \cdot \varepsilon_{e,\mathbf{G}\mathbf{G}'}^{-1} \cdot \chi_{\text{lat},\mathbf{G}\mathbf{G}'} \cdot \varepsilon_{e,\mathbf{G}\mathbf{G}'}^{-1} \quad (5.4)$$

where the only requirement is that  $\varepsilon_{e,\mathbf{G}\mathbf{G}'}$  is invertible. The lattice susceptibility matrix is only non-zero in the head ( $\mathbf{G} = 0, \mathbf{G}' = 0$ ) element. The total dielectric function is now expressed as the conventional electronic contribution and an extra term, which is the corrective term. The inverse of the electronic dielectric matrix is already available and thus taking the inverse here will not be necessary. The element  $\varepsilon_{e,00}^{-1}$ , as an example,

represents the  $\mathbf{G} = 0, \mathbf{G}' = 0$  element of the inverted electronic dielectric matrix.

Consider first the matrix product  $\chi_{\text{lat}, \mathbf{G}\mathbf{G}'} \cdot \epsilon_{\mathbf{e}, \mathbf{G}\mathbf{G}'}^{-1}$ , which results in a single non-zero row, due to the fact that the only non-zero element in  $\chi_{\text{lat}, \mathbf{G}\mathbf{G}'}$  is the head element (i.e.  $\chi_{\text{lat}, 00} \neq 0$ ). This matrix product reads as

$$\chi_{\text{lat}, \mathbf{G}\mathbf{G}'} \cdot \epsilon_{\mathbf{e}, \mathbf{G}\mathbf{G}'}^{-1} = \begin{bmatrix} \chi_{\text{lat}, 00} \cdot \epsilon_{\mathbf{e}, 00}^{-1} & \chi_{\text{lat}, 00} \cdot \epsilon_{\mathbf{e}, 01}^{-1} & \chi_{\text{lat}, 00} \cdot \epsilon_{\mathbf{e}, 02}^{-1} & \cdots \\ 0 & 0 & 0 & \cdots \\ 0 & 0 & 0 & \cdots \\ \vdots & \vdots & \vdots & \ddots \end{bmatrix}, \quad (5.5)$$

where it is clear that the trace present in equation (5.4) is simply the head of the above matrix. Now consider the matrix product proposed by Botti and Marques [13]

$$\epsilon_{\mathbf{e}, \mathbf{G}0}^{-1} \cdot \chi_{\text{lat}, 00} \cdot \epsilon_{\mathbf{e}, 0\mathbf{G}'}^{-1} = \begin{bmatrix} \epsilon_{\mathbf{e}, 00}^{-1} & \epsilon_{\mathbf{e}, 01}^{-1} & \epsilon_{\mathbf{e}, 02}^{-1} & \cdots \\ \epsilon_{\mathbf{e}, 10}^{-1} & \epsilon_{\mathbf{e}, 11}^{-1} & \epsilon_{\mathbf{e}, 12}^{-1} & \cdots \\ \epsilon_{\mathbf{e}, 20}^{-1} & \epsilon_{\mathbf{e}, 21}^{-1} & \epsilon_{\mathbf{e}, 22}^{-1} & \cdots \\ \vdots & \vdots & \vdots & \ddots \end{bmatrix} \cdot \chi_{\text{lat}, 00} \cdot \begin{bmatrix} \epsilon_{\mathbf{e}, 00}^{-1} & \epsilon_{\mathbf{e}, 01}^{-1} & \epsilon_{\mathbf{e}, 02}^{-1} & \cdots \\ \epsilon_{\mathbf{e}, 10}^{-1} & \epsilon_{\mathbf{e}, 11}^{-1} & \epsilon_{\mathbf{e}, 12}^{-1} & \cdots \\ \epsilon_{\mathbf{e}, 20}^{-1} & \epsilon_{\mathbf{e}, 21}^{-1} & \epsilon_{\mathbf{e}, 22}^{-1} & \cdots \\ \vdots & \vdots & \vdots & \ddots \end{bmatrix} \quad (5.6)$$

$$= \begin{bmatrix} \epsilon_{\mathbf{e}, 00}^{-1} \cdot \chi_{\text{lat}, 00} \cdot \epsilon_{\mathbf{e}, 00}^{-1} & \epsilon_{\mathbf{e}, 00}^{-1} \cdot \chi_{\text{lat}, 00} \cdot \epsilon_{\mathbf{e}, 01}^{-1} & \epsilon_{\mathbf{e}, 00}^{-1} \cdot \chi_{\text{lat}, 00} \cdot \epsilon_{\mathbf{e}, 02}^{-1} & \cdots \\ \epsilon_{\mathbf{e}, 10}^{-1} \cdot \chi_{\text{lat}, 00} \cdot \epsilon_{\mathbf{e}, 00}^{-1} & \epsilon_{\mathbf{e}, 10}^{-1} \cdot \chi_{\text{lat}, 00} \cdot \epsilon_{\mathbf{e}, 01}^{-1} & \epsilon_{\mathbf{e}, 10}^{-1} \cdot \chi_{\text{lat}, 00} \cdot \epsilon_{\mathbf{e}, 02}^{-1} & \cdots \\ \epsilon_{\mathbf{e}, 20}^{-1} \cdot \chi_{\text{lat}, 00} \cdot \epsilon_{\mathbf{e}, 00}^{-1} & \epsilon_{\mathbf{e}, 20}^{-1} \cdot \chi_{\text{lat}, 00} \cdot \epsilon_{\mathbf{e}, 01}^{-1} & \epsilon_{\mathbf{e}, 20}^{-1} \cdot \chi_{\text{lat}, 00} \cdot \epsilon_{\mathbf{e}, 02}^{-1} & \cdots \\ \vdots & \vdots & \vdots & \ddots \end{bmatrix}, \quad (5.7)$$

which is identical to the matrix product  $\epsilon_{\mathbf{e}, \mathbf{G}\mathbf{G}'}^{-1} \cdot \chi_{\text{lat}, \mathbf{G}\mathbf{G}'} \cdot \epsilon_{\mathbf{e}, \mathbf{G}\mathbf{G}'}^{-1}$  present in equation (5.4). This simplification is motivated by the fact that extracting only the wing elements,  $\mathbf{G}0$  and  $0\mathbf{G}'$ , means that not all elements have to be evaluated. which will simplify the analysis and ultimately decrease the computational calculation time. This results in the following simplified total dielectric matrix

$$\epsilon_{\mathbf{G}\mathbf{G}'}^{-1} = \epsilon_{\mathbf{e}, \mathbf{G}\mathbf{G}'}^{-1} - \frac{1}{1 + \chi_{\text{lat}, 00} \cdot \epsilon_{\mathbf{e}, 00}^{-1}} \cdot \epsilon_{\mathbf{e}, \mathbf{G}0}^{-1} \cdot \chi_{\text{lat}, 00} \cdot \epsilon_{\mathbf{e}, 0\mathbf{G}'}^{-1}, \quad (5.8)$$

which can be implemented into the GW formalism.

## 5.2. Analytic Solution to the Self-Energy

As a start only the head of the total dielectric matrix will be considered for a simpler analysis. The corrective term in equation (5.8), which will be dubbed the dielectric lattice correction ( $\tilde{\epsilon}_{\text{lat}, \mathbf{G}\mathbf{G}'}^{-1}$ ), due to its appearance deriving from the inclusion of lattice contributions, can be identified as

$$\tilde{\epsilon}_{\text{lat}, 00}^{-1} = -\frac{1}{1 + \chi_{\text{lat}, 00} \cdot \epsilon_{\mathbf{e}, 00}^{-1}} \cdot \epsilon_{\mathbf{e}, 00}^{-1} \cdot \chi_{\text{lat}, 00} \cdot \epsilon_{\mathbf{e}, 00}^{-1} \quad (5.9)$$

$$= -\epsilon_{\mathbf{e}, 00}^{-1} \cdot \frac{1}{\epsilon_{\mathbf{e}, 00} + \chi_{\text{lat}, 00}} \cdot \chi_{\text{lat}, 00}. \quad (5.10)$$

The true lattice dielectric function is of course  $\epsilon_{\text{lat}} = 1 + \chi_{\text{lat}}$ . The lattice susceptibility is expressed as in equation (4.21) for a single mode, the TO phonon mode, and in terms of the effective Born-charge. The electronic dielectric can be approximated to a constant value,  $\epsilon_{\mathbf{e}, 00} = \epsilon_{\infty}$ , in the infrared frequency regime where lattice contributions occur. As seen in figure 1.1, this requires a sufficiently large band-gap to separate the lattice and

electronic contributions. This is safe to assume in semiconductor materials. Utilising this and substituting the susceptibility, the lattice correction can then be expressed as

$$\tilde{\varepsilon}_{\text{lat},00}^{-1} = -\varepsilon_{\infty}^{-1} \left( \Omega_{\text{cell}} \frac{(\omega_{TO} + (\omega + i\eta))(\omega_{TO} - (\omega + i\eta))}{4\pi\bar{Z}^2} \varepsilon_{\infty} + 1 \right)^{-1}. \quad (5.11)$$

It is of interest to express the above in a form where simple poles are present, in order to ultimately solve the self-energy integral, equation (3.15), by contour integration. In order to do so a system of linear equations is constructed by expressing the polynomial in a linear combination of different order terms.

$$(a(\omega + i\eta) - \omega_{\alpha})(b(\omega + i\eta) - \omega_{\beta}) = \Omega_{\text{cell}} \frac{(\omega_{TO} + (\omega + i\eta))(\omega_{TO} - (\omega + i\eta))}{4\pi\bar{Z}^2} \varepsilon_{\infty} + 1, \quad (5.12)$$

allows for the following system of equations by equating terms with the same order in  $\omega$  from the left hand side and right hand side.

$$0^{\text{th}} \text{ order : } \quad \omega_{\alpha}\omega_{\beta} = 1 + \frac{\varepsilon_{\infty}\Omega_{\text{cell}}}{4\pi\bar{Z}^2} \omega_{TO}^2. \quad (5.13)$$

$$1^{\text{st}} \text{ order : } \quad -(a(\omega + i\eta)\omega_{\beta} + b(\omega + i\eta)\omega_{\alpha}) = 0. \quad (5.14)$$

$$2^{\text{nd}} \text{ order : } \quad ab(\omega + i\eta)^2 = -\frac{\varepsilon_{\infty}\Omega_{\text{cell}}}{4\pi\bar{Z}^2} (\omega + i\eta)^2. \quad (5.15)$$

This presents three equations with four unknowns:  $\omega_{\alpha}$ ,  $\omega_{\beta}$ ,  $a$ , and  $b$ . Setting  $a = 1$ , the system of equations can be solved

$$\begin{aligned} b((\omega + i\eta) - \omega_{\alpha})((\omega + i\eta) - \frac{\omega_{\beta}}{b}) \\ = -\frac{\varepsilon_{\infty}\Omega_{\text{cell}}}{4\pi\bar{Z}^2} \left( (\omega + i\eta) - \frac{4\pi\bar{Z}^2}{\varepsilon_{\infty}\Omega_{\text{cell}}} \sqrt{\frac{\varepsilon_{\infty}\Omega_{\text{cell}}}{4\pi\bar{Z}^2} \left( 1 + \frac{\varepsilon_{\infty}\Omega_{\text{cell}}}{4\pi\bar{Z}^2} \omega_{TO}^2 \right)} \right) \\ \times \left( (\omega + i\eta) + \frac{4\pi\bar{Z}^2}{\varepsilon_{\infty}\Omega_{\text{cell}}} \sqrt{\frac{\varepsilon_{\infty}\Omega_{\text{cell}}}{4\pi\bar{Z}^2} \left( 1 + \frac{\varepsilon_{\infty}\Omega_{\text{cell}}}{4\pi\bar{Z}^2} \omega_{TO}^2 \right)} \right). \end{aligned} \quad (5.16)$$

The lattice correction can now be expressed as

$$\tilde{\varepsilon}_{\text{lat},00}^{-1} = \frac{4\pi\bar{Z}^2}{\varepsilon_{\infty}^2\Omega_{\text{cell}}} \left( (\omega + i\eta)^2 - \left( \omega_{TO}^2 + \frac{4\pi\bar{Z}^2}{\varepsilon_{\infty}\Omega_{\text{cell}}} \right) \right)^{-1}. \quad (5.17)$$

Inserting the total dielectric function from equation (5.8) including the lattice correction term in equation (5.17) as

$$\varepsilon_{00}^{-1} = \varepsilon_{e,00}^{-1} + \tilde{\varepsilon}_{\text{lat},00}^{-1}, \quad (5.18)$$

into the GW self-energy integral results in a splitting of the integral into the conventional electronic part,  $\Sigma_e$  and a part involving the lattice correction,  $\tilde{\Sigma}_{\text{lat}}$ , where  $\sim$  will continue to denote the correction term due to lattice contributions. Referring to equation (3.15), the GW self-energy can now be expressed as

$$\begin{aligned} \langle \phi_{n\mathbf{k}}^{\text{KS}} | \Sigma(\omega) | \phi_{n\mathbf{k}}^{\text{KS}} \rangle = \frac{1}{\Omega} \sum_{\mathbf{q}} \sum_m \frac{i}{2\pi} \int_{-\infty}^{\infty} d\omega' \frac{\rho_{m\mathbf{k}-\mathbf{q}}^{n\mathbf{k}}(\mathbf{q}) \rho_{m\mathbf{k}-\mathbf{q}}^{*n\mathbf{k}}(\mathbf{q})}{\omega + \omega' - \varepsilon_{m\mathbf{k}-\mathbf{q}}^{\text{KS}} + i\eta \text{sgn}(\varepsilon_{m\mathbf{k}-\mathbf{q}}^{\text{KS}} - \mu)} \\ \times \left( W_{e,00}(\mathbf{q}, \omega') + \tilde{W}_{\text{lat},00}(\mathbf{q}, \omega') \right) \end{aligned} \quad (5.19)$$

where

$$\tilde{W}_{\text{lat},00}(\mathbf{q}, \omega') = \tilde{\varepsilon}_{\text{lat},00}^{-1}(\mathbf{q}, \omega') \frac{4\pi}{|\mathbf{q}|^2} \quad (5.20)$$

is the lattice correction to the screened Coulomb interaction. Since the integral involving  $W_{e,00}(\mathbf{q}, \omega')$  is the usual GW integral discussed in section 3.2, the focus lies on this correction term

$$\begin{aligned} \langle \phi_{n\mathbf{k}}^{\text{KS}} | \tilde{\Sigma}_{\text{lat}}(\omega) | \phi_{n\mathbf{k}}^{\text{KS}} \rangle &= \frac{2i}{\Omega} \frac{4\pi \bar{Z}^2}{\varepsilon_{\infty}^2 \Omega_{\text{cell}}} \sum_{\mathbf{q}} \sum_m^{\text{B.Z.}} \frac{\rho_{m\mathbf{k}-\mathbf{q}}^{n\mathbf{k}}(\mathbf{q}) \rho_{m\mathbf{k}-\mathbf{q}}^{*n\mathbf{k}}(\mathbf{q})}{|\mathbf{q}|^2} \\ &\times \int_{-\infty}^{\infty} d\omega' \frac{1}{\omega + \omega' - \varepsilon_{m\mathbf{k}-\mathbf{q}}^{\text{KS}} + i\eta \operatorname{sgn}(\varepsilon_{m\mathbf{k}-\mathbf{q}}^{\text{KS}} - \mu)} \\ &\times \frac{1}{(\omega' + i\eta)^2 - \left( \omega_{\text{TO}}^2 + \frac{4\pi \bar{Z}^2}{\varepsilon_{\infty} \Omega_{\text{cell}}} \right)}, \end{aligned} \quad (5.21)$$

which corrects the total self-energy by

$$\langle \phi_{n\mathbf{k}}^{\text{KS}} | \Sigma(\omega) | \phi_{n\mathbf{k}}^{\text{KS}} \rangle = \langle \phi_{n\mathbf{k}}^{\text{KS}} | \left( \Sigma_e(\omega) + \tilde{\Sigma}_{\text{lat}}(\omega) \right) | \phi_{n\mathbf{k}}^{\text{KS}} \rangle. \quad (5.22)$$

The frequency integral present can be solved using the residue theorem, which states that the integral of a function around a closed contour in the complex plane is  $2\pi i$  times the sum over the residues at poles enclosed by the contour. This is expressed as

$$\oint_C dz f(z) = 2\pi i \sum_k \operatorname{Res}\{f, z_k\} \quad (5.23)$$

where  $k$  denotes the poles. The integrand of equation (5.21) reads

$$f(\omega') = \frac{1}{\omega + \omega' - \varepsilon_{m\mathbf{k}-\mathbf{q}}^{\text{KS}} + i\eta \operatorname{sgn}(\varepsilon_{m\mathbf{k}-\mathbf{q}}^{\text{KS}} - \mu)} \cdot \frac{1}{(\omega' + i\eta)^2 - \left( \omega_{\text{TO}}^2 + \frac{4\pi \bar{Z}^2}{\varepsilon_{\infty} \Omega_{\text{cell}}} \right)} \quad (5.24)$$

and has poles at

$$\omega' = \omega_0 = -\omega + \varepsilon_{m\mathbf{k}-\mathbf{q}}^{\text{KS}} + i\eta \quad , \quad \sqrt{\omega_{\text{TO}}^2 + \frac{4\pi \bar{Z}^2}{\varepsilon_{\infty} \Omega_{\text{cell}}}} - i\eta \quad (5.25)$$

where only poles due to occupied bands are considered so that  $\operatorname{sgn}(\varepsilon_{m\mathbf{k}-\mathbf{q}}^{\text{KS}} - \mu)$  is negative, as the Kohn-Sham energies will situate below the chemical potential. A contour integral is chosen in the upper half plane, and thus only poles in the upper half plane will contribute to the evaluation. The residue of the integrand is

$$\operatorname{Res}\{f, \omega_0\} = \lim_{\omega' \rightarrow \omega_0} (\omega' - \omega_0) \cdot f(\omega') \quad ; \quad \omega_0 = -\omega + \varepsilon_{m\mathbf{k}-\mathbf{q}}^{\text{KS}} + i\eta \quad (5.26)$$

$$= \left( \left( -\omega + \varepsilon_{m\mathbf{k}-\mathbf{q}}^{\text{KS}} + i\eta \right)^2 - \left( \omega_{\text{TO}}^2 + \frac{4\pi \bar{Z}^2}{\varepsilon_{\infty} \Omega_{\text{cell}}} \right) \right)^{-1} \quad (5.27)$$

$$= \left( \left( \omega - \varepsilon_{m\mathbf{k}-\mathbf{q}}^{\text{KS}} - i\eta \right)^2 - \left( \omega_{\text{TO}}^2 + \frac{4\pi \bar{Z}^2}{\varepsilon_{\infty} \Omega_{\text{cell}}} \right) \right)^{-1}. \quad (5.28)$$



When applying the residue theorem a solution arises that reads

$$\int_{-\infty}^{\infty} d\omega' f(\omega') = 2\pi i \left( \left( \omega - \varepsilon_{m\mathbf{k}-\mathbf{q}}^{\text{KS}} - i\eta \right)^2 - \left( \omega_{\text{TO}}^2 + \frac{4\pi\bar{Z}^2}{\varepsilon_{\infty}\Omega_{\text{cell}}} \right) \right)^{-1}. \quad (5.29)$$

Inserting a step function ensures the sum over bands includes occupied bands only, since the complex contour integral was solved only for occupied bands. This results in

$$\begin{aligned} \langle \phi_{n\mathbf{k}}^{\text{KS}} | \tilde{\Sigma}_{\text{lat}}(\omega) | \phi_{n\mathbf{k}}^{\text{KS}} \rangle = & - \left( \frac{4\pi\bar{Z}}{\varepsilon_{\infty}} \right)^2 \frac{1}{\Omega_{\text{cell}}} \frac{1}{\Omega} \sum_{\mathbf{q}}^{\text{B.Z.}} \sum_m \frac{\rho_{m\mathbf{k}-\mathbf{q}}^{n\mathbf{k}}(\mathbf{q}) \rho_{m\mathbf{k}-\mathbf{q}}^{*n\mathbf{k}}(\mathbf{q})}{|\mathbf{q}|^2} \\ & \times \frac{\Theta(\mu - \varepsilon_{m\mathbf{k}-\mathbf{q}}^{\text{KS}})}{\left( \omega - \varepsilon_{m\mathbf{k}-\mathbf{q}}^{\text{KS}} - i\eta \right)^2 - \left( \omega_{\text{TO}}^2 + \frac{4\pi\bar{Z}^2}{\varepsilon_{\infty}\Omega_{\text{cell}}} \right)}, \end{aligned} \quad (5.30)$$

which presents an analytic expression of the dynamic lattice corrections to the GW quasi-particle energies.

### 5.2.1. Revisiting the Vanishing $\mathbf{q}$ Limit

An analytic solution to a corrective lattice contributing term in the GW self-energy is present in equation (5.30). The sum over  $\mathbf{q}$  in this expression requires special attention due to the divergence of  $1/|\mathbf{q}|^2$  in the  $\mathbf{q} \rightarrow 0$  limit. This means that the term,

$$\frac{1}{\Omega} \sum_{\mathbf{q}} \frac{|\rho_{m\mathbf{k}-\mathbf{q}}^{n\mathbf{k}}(\mathbf{q})|^2}{|\mathbf{q}|^2}, \quad (5.31)$$

must be treated applying knowledge from sub-section 3.2.1. In the vanishing limit the contribution to the sum over  $\mathbf{q}$  is converted to an integral as,

$$\frac{1}{\Omega} \sum_{\mathbf{q}} \rightarrow \frac{1}{\Omega} \left( \frac{\Omega}{(2\pi)^3} \int_{V_{\mathbf{q}=0}} dq \, 4\pi q^2 + \sum_{\mathbf{q}'} \frac{|\rho_{m\mathbf{k}-\mathbf{q}'}^{n\mathbf{k}}(\mathbf{q}')|^2}{|\mathbf{q}'|^2} \right), \quad (5.32)$$

in order to obtain a finite value upon integrating the  $q$ -dependency over a sphere encompassing the origin denoted by,  $V_{\mathbf{q}=0}$ . Here  $\mathbf{q}'$  defines a sum over the remaining  $\mathbf{q}$ -points (i.e. excluding the  $\mathbf{q} = 0$ /origin point). Applying equation (3.21), an expression for the pair-density in the  $\mathbf{q} \rightarrow 0$  limit, the integral about the origin then reads

$$\frac{1}{\Omega} \frac{\Omega}{(2\pi)^3} \int_{V_{\mathbf{q}=0}} dq \left| \delta_{nm} - i\mathbf{q} \cdot \frac{\langle u_{n\mathbf{k}} | (\nabla + i\mathbf{k}) | u_{m\mathbf{k}} \rangle}{\varepsilon_{m\mathbf{k}} - \varepsilon_{n\mathbf{k}}} \right|^2 \frac{4\pi q^2}{|\mathbf{q}|^2}, \quad (5.33)$$

and when defining

$$\mathbf{C} = i \frac{\langle u_{n\mathbf{k}} | (\nabla + i\mathbf{k}) | u_{m\mathbf{k}} \rangle}{\varepsilon_{m\mathbf{k}} - \varepsilon_{n\mathbf{k}}}, \quad (5.34)$$

the divergent term, with a sphere of radius,  $q_r$  around the divergence, results in

$$\frac{1}{\Omega} \sum_{\mathbf{q}} \frac{|\rho_{m\mathbf{k}-\mathbf{q}}^{n\mathbf{k}}(\mathbf{q})|^2}{|\mathbf{q}|^2} \approx \frac{4\pi}{(2\pi)^3} \int_0^{q_r} dq \, |\delta_{nm} - \mathbf{q} \cdot \mathbf{C}|^2 + \frac{1}{\Omega} \sum_{\mathbf{q}'} \frac{|\rho_{m\mathbf{k}-\mathbf{q}'}^{n\mathbf{k}}(\mathbf{q}')|^2}{|\mathbf{q}'|^2}. \quad (5.35)$$

The Kronecker-delta presents two separate solutions for the diagonal terms and off-diagonal terms. For  $n = m$ , the Kronecker-delta is unity and dominates in the integral, since  $\mathbf{q} \rightarrow 0$ , and for  $n \neq m$ , only  $\mathbf{q} \cdot \mathbf{C}$  remains. The solutions to the integral for the two cases are

$$\frac{4\pi}{(2\pi)^3} \int_0^{q_r} dq |\delta_{nm} - \mathbf{q} \cdot \mathbf{C}|^2 \approx \begin{cases} \frac{4\pi}{(2\pi)^3} \int_0^{q_r} dq = \frac{4\pi}{(2\pi)^3} q_r & ; n = m \\ \frac{4\pi}{(2\pi)^3} \int_0^{q_r} dq |-\mathbf{q} \cdot \mathbf{C}|^2 = \frac{4\pi}{(2\pi)^3} \frac{1}{3} q_r^3 \cdot |\mathbf{C}|^2 & ; n \neq m \end{cases} \quad (5.36)$$

The miniscule spherical volume about a  $\mathbf{q}$ -point, with radius  $q_r$ , can be expressed by dividing the Brillouin-Zone volume,  $\Omega_{\text{BZ}}$  ( $= (2\pi)^3/\Omega_{\text{cell}}$ ), by the number of  $\mathbf{q}$ -points,  $N_q$ . An expression for  $q_r$  in this limit can be obtained by equating this to the volume of a sphere. This reads as

$$\frac{\Omega_{\text{BZ}}}{N_q} = \frac{4\pi}{3} q_r^3 \rightarrow q_r = \left( \frac{3}{4\pi} \frac{\Omega_{\text{BZ}}}{N_q} \right)^{1/3}, \quad (5.37)$$

which provides the following solutions to equation (5.35) for the  $\mathbf{q}$ -dependent terms in the  $\mathbf{q} \rightarrow 0$  limit.

$$\frac{|\rho_{m\mathbf{k}-\mathbf{q}}^{n\mathbf{k}}(\mathbf{q})|^2}{|\mathbf{q}|^2} \approx \begin{cases} \frac{4\pi}{(2\pi)^3} q_r = \frac{1}{4\pi^2} \left( \frac{48\pi^2}{\Omega_{\text{cell}} N_q} \right)^{1/3} & ; n = m \\ \frac{4\pi}{(2\pi)^3} \frac{1}{3} q_r^3 \cdot |\mathbf{C}|^2 = \frac{|\mathbf{C}|^2}{\Omega_{\text{cell}} N_q} & ; n \neq m \end{cases} \quad (5.38)$$

This solution closes the divergence at  $\mathbf{q} = 0$ . For finite- $\mathbf{q}$ , equation (5.30) is well-behaved, and thus requires no extra attention. The full solution can be implemented into GW code to correct band-structures that currently only involve the electronic contributions.

## Implementation as an Atomic Simulation Recipe

The lattice correction is implemented as a post-processing tool to GW calculations. This implies that a typical GW calculation should be executed prior to calculating the lattice correction to the self-energy. Several variables must be extracted in order to calculate the correction, as seen in equation (5.30). This includes pair-densities, effective Born-charges, the electronic dielectric constant in the infrared frequency regime, phonon frequency modes, and Kohn-Sham eigen-energies, all of which are available for extraction from various GPAW calculations. This chapter will briefly describe the extraction of these variables from existing modules, however the focus will be on the numerical implementation of equation (5.30). The code developed for this will be a part of the Atomic Simulation Recipes (ASR) package. ASR is currently under development and will add to the existing Atomic Simulation Environment (ASE), *"a set of tools and Python modules for setting up, manipulating, running, visualising and analysing atomistic simulations"* [25]. The aim of ASR is to create a *"collection of python recipes for common (and not so common) tasks performed in atomic scale materials research"* [26]. These Python recipes are Python modules that can be run by any user, without requiring any manual input. The overall work-flow, along with the desired variables and files is presented in figure 6.1. As mentioned, the final step of this work-flow is the focus of the project, whereas the first two levels already exist as working recipes.

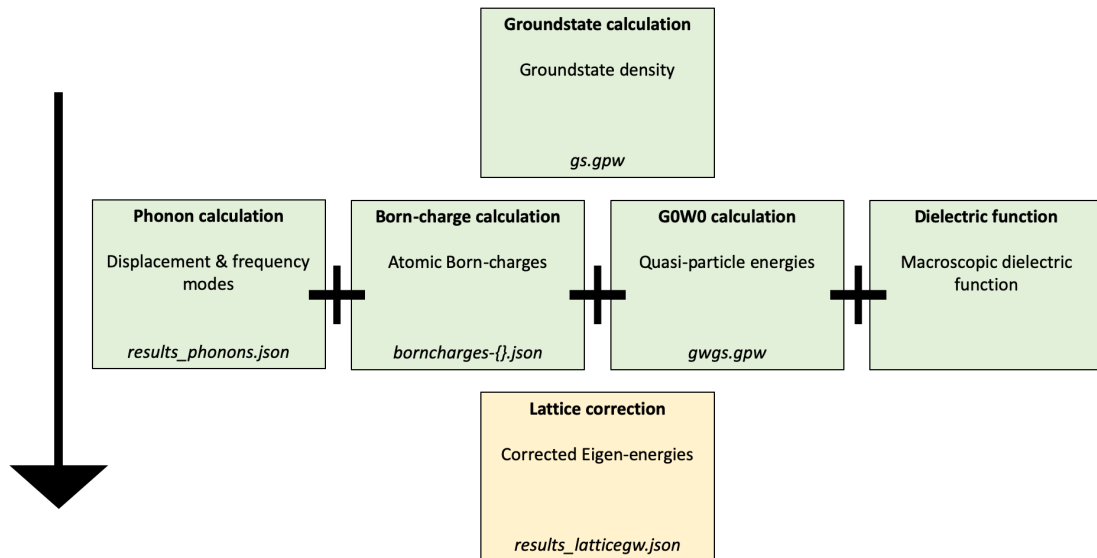


Figure 6.1: Workflow for the implementation of calculating lattice corrections to GW band-structures. Green represents existing recipes and yellow the recipe in focus for this work.

## 6.1. Prerequisite Variables from Existing Recipes

All boxes in figure 6.1 coloured in green represent existing Python recipes and modules. The recipe constructed for the lattice corrections depends on these, and the following will describe which dependencies come from which module/recipe.

As a start, the lattice correction recipe will require a typical DFT ground-state calculation. This primarily obtains the ground-state density, along with atomic forces and the stress tensors, which is saved into a *gs.gpw* file in order to be implemented into other modules. The ground-state recipe available in ASR, only requires the atomic structure as input. By default the plane-wave energy cut-off is set to 800 eV, with a  $\mathbf{k}$ -point density of 6 pts/ $\text{\AA}^{-3}$  using the PBE exchange-correlation functional. Utilising the *gs.gpw* file, the phonon recipe can read eigen-frequencies and displacement modes, and the GW calculator can utilise the density and thus effective potential from the DFT calculation.

ASE provides a module for calculating vibrational normal modes, i.e. phonons, of periodic systems. This is based on the '*small displacement*' method proposed by Alfe *et al.* [27]. eigen-modes and -frequencies are available from the calculation via the dynamical matrix introduced in section 4. Phonon frequency modes are only desired at the  $\Gamma$ -point. This can be achieved by setting a path to the phonon calculation, in this case  $[0, 0, 0]$  for the  $\Gamma$ -point. Using ASE's *.band\_structure()* function, the frequencies and displacement of all modes can be extracted for a given path.

A recipe is also available for the Born-charges, which displaces each atom in the structure individually in all Cartesian directions and calculates the change in polarisation density in all Cartesian directions via a Berry-phase arising from the displacement [24]. The Born-charge can thus be calculated by differentiating the induced polarisation density with respect to the displacement. The default displacement is 0.01  $\text{\AA}$ , and the default  $\mathbf{k}$ -point density for the Berry-phase calculation is 6 pts/ $\text{\AA}^{-3}$ . As expressed in equation (4.20), the effective Born-charge is the dot product between the atomic Born-charge and displacement mode of the dynamical matrix, which is available from the phonon calculation previously described. Section 4 described a single-mode approximation to the expansion of the dynamical matrix. The largest contributing Born-charge is obtained by scanning for the maximum Born-charge of all modes. This is then also the mode of the phonon frequency, which can be assumed to be the TO frequency.

Finally, Kohn-Sham transition energies and pair-densities are available for extraction from the GW calculation, which is also an existing module. The GW calculation requires the definition of a GPAW calculator, which specifies primarily the number of bands to be included, the  $\mathbf{k}$ -point density, and toggles the fixed density method, applying the density obtained from the DFT calculation. The GW calculation stores its results in a *gwgs.gpw* file, which can subsequently be loaded into the *DielectricFunction()* module, for calculating the macroscopic dielectric function.

## 6.2. Recipe for GW Corrections from Lattice Contributions

As implied in equation (5.30), the correction is evaluated for a specific band,  $n$ , and  $\mathbf{k}$ -point at a time, and for each, contributions from every occupied band,  $m$ , and  $\mathbf{q}$ -point are summed over.

Pair-densities and Kohn-Sham eigen-energies are extracted using a GPAW calculator. Both are dependent on the respective  $\mathbf{k}$ -point and band. The GPAW calculator defines the number of bands and  $\mathbf{k}$ -points in the calculation. This calculator, as mentioned, can be defined by the *gwgs.gpw* file from the GW calculation, however since the lattice correction

is a relatively quick calculation, it is possible to increase the number of **k**-points for a more accurate set of corrections. This allows for a new GPAW calculator to be defined with an increased **k**-point sampling. Along with this, the **k**-point grid is set to sample the  $\Gamma$ -point and maintain an even number of **k**-points in all directions. The number of un-occupied bands is set to 10, and converged up to the last 5. The **q**-point grid is successively defined by extracting the constructed **k**-point grid and applying an offset to avoid the **q** = 0 point. This means the **q**-point density is adjusted by the **k**-point density.

The pair-densities are extracted using the `.get_pair_density()` function, with the specified GPAW calculator. Just as it was necessary to handle the **q**-limits of equation (5.30), the pair-densities must also be treated properly in the code. For finite-**q** the function returns  $\rho_{m\mathbf{k}-\mathbf{q}}^n(\mathbf{q})$ , which can be implemented directly into the expression. However in the  $\mathbf{q} \rightarrow 0$  limit, the function returns the expression in equation (3.21), and thus the solutions in equation (5.38), for the  $n = m$  and  $n \neq m$  cases to the **q**-limit, must be applied accordingly. This is presented in pseudo-Python code in listing 6.1, where a factor of  $1/\Omega_{\text{cell}}N_q$  is pulled out of equation (5.38). The pair-densities extracted have a dimension representing the  $x$ ,  $y$  and  $z$  directions in reciprocal space. In the  $\mathbf{q} \rightarrow 0$  limit, only the **q** = 0 point is involved and the pair-density does not necessarily approach **q** = 0 identically from all directions. To treat this an average is taken over the three directions in the  $\mathbf{q} \rightarrow 0$  limit. Otherwise for finite-**q**, the direction is set by **q**.

```

1 # extract pair-density for fixed k and q.
2 # n - all bands, m - valence bands, v - Cartesian directions.
3 if q → 0 limit:
4     ρn,m,v = pair.get_pair_density()
5     ρn,m2 = ∑v |ρn,m,v|2 / 3 # n ≠ m terms
6     ρm,m2 = ( 1 / ((4 * π2) * (48 * π2 / (Ωcell * Nq))1/3) ) * (Ωcell * Nq) # n = m terms
7 else finite-q:
8     ρn,m = pair.get_pair_density()
9     ρn,m2 = |ρn,m|2 / |q|2 # finite q terms

```

Listing 6.1: Pseudo-Python code treatment of pair-densities.

Equation (5.30) is in practice evaluated at the eigen-energy of the corresponding eigenstates in the evaluation ( $\omega = \epsilon_{n\mathbf{k}}^{\text{KS}}$ ), and thus the Kohn-Sham transition energies,  $\epsilon_{n\mathbf{k}}^{\text{KS}} - \epsilon_{m\mathbf{k}-\mathbf{q}}^{\text{KS}}$  can be extracted using the `.get_transition_energies()` function.

### 6.3. Treating Numerical Singularities

It is noticeable that divergences will occur in equation (5.30) depending on the numerical evaluation with a discrete **k**-point sampling. These divergences occur when

$$\left(\epsilon_{n\mathbf{k}}^{\text{KS}} - \epsilon_{m\mathbf{k}-\mathbf{q}}^{\text{KS}} - i\eta\right)^2 = \omega_{\text{TO}}^2 + \frac{4\pi\bar{Z}^2}{\epsilon_{\infty}\Omega_{\text{cell}}} \quad (6.1)$$

which appears in the denominator of equation (5.30) and is clearly dependent on the **k**-points defining the energies. A coarse sampling may miss the singularity, but regardless these singularities require special treatment to avoid divergence peaks in the results.

#### 6.3.1. Microvolume Integration

Closing the singularities can be achieved by integration of cylindrical micro-volumes assigned to each **q**-point. Utilising a cylinder introduces two variables, the radius,  $q_r$ , and

length,  $q_z$ , of the cylinder, which are free variables and their fitting based on the available  $\mathbf{q}$ -points will be described. This is depicted in figure 6.2 for an arbitrary  $\mathbf{k}/\mathbf{q}$ -point pair.

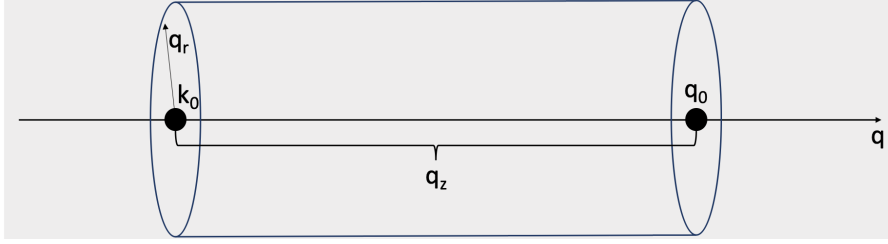


Figure 6.2: Illustration of cylindrical micro-volume for closing singularities.

For a fixed band,  $n$  and  $\mathbf{k}$ -point equation (5.30) is re-written as

$$\langle \phi_{n\mathbf{k}}^{\text{KS}} | \tilde{\Sigma}_{\text{lat}}(\omega) | \phi_{n\mathbf{k}}^{\text{KS}} \rangle = - \left( \frac{4\pi\bar{Z}}{\varepsilon_\infty} \right)^2 \frac{1}{\Omega_{\text{cell}}} \frac{1}{\Omega} \sum_{\mathbf{q}}^{\text{B.Z.}} \sum_m G_m(\mathbf{q}) H_m(\mathbf{q}) \quad (6.2)$$

where

$$G_m(\mathbf{q}) = \frac{\rho_{m\mathbf{k}-\mathbf{q}}^{n\mathbf{k}} \rho_{m\mathbf{k}-\mathbf{q}}^{*n\mathbf{k}}}{|\mathbf{q}|^2}, \quad (6.3)$$

$$H_m(\mathbf{q}) = \frac{1}{\left( \varepsilon_{n\mathbf{k}}^{\text{KS}} - \varepsilon_{m\mathbf{k}-\mathbf{q}}^{\text{KS}} - i\eta \right)^2 - \left( \omega_{\text{TO}}^2 + \frac{4\pi\bar{Z}^2}{\varepsilon_\infty\Omega_{\text{cell}}} \right)}, \quad (6.4)$$

for semiconductor/insulator systems where the electrons fill the valence bands and so  $\Theta(\mu - \varepsilon_{m\mathbf{k}-\mathbf{q}}^{\text{KS}}) = 1$ . The sum over  $\mathbf{q}$ -points within the Brillouin-Zone can be converted to a 3-Dimensional volume integral over the Brillouin-Zone.

$$\sum_{\mathbf{q}}^{\text{B.Z.}} \approx \frac{1}{V_q} \int_{\text{B.Z.}} d^3q \quad (6.5)$$

where the volume is expressed as

$$V_q = \frac{\Omega_{\text{BZ}}}{N_q} = \frac{(2\pi)^3}{\Omega_{\text{cell}} N_q}. \quad (6.6)$$

which, when inserting equations (6.5) and (6.6) into (6.2), leads to the following expression for the lattice correction.

$$\langle \phi_{n\mathbf{k}}^{\text{KS}} | \tilde{\Sigma}_{\text{lat}}(\omega) | \phi_{n\mathbf{k}}^{\text{KS}} \rangle = - \left( \frac{4\pi\bar{Z}}{\varepsilon_\infty} \right)^2 \frac{N_q}{\Omega(2\pi)^3} \sum_m \int_{\text{B.Z.}} d^3q G_m(\mathbf{q}) H_m(\mathbf{q}). \quad (6.7)$$

In order to proceed with solving the integral, the Brillouin-Zone is divided into segments defined by a point  $q_i$ , where  $i$  denotes the segment, and a miniscule translation from this point  $\tilde{q}$ , which assigns a volume to each point. This is illustrated in figure 6.3a for a 2-Dimensional grid (however the idea extends in 3-Dimensions, presenting volumes instead of areas). The volume assigned to each point is determined by dividing the Brillouin-Zone volume into the number of  $\mathbf{q}$ -points. The expression now involves a sum over segments described by a volume integral. The function  $G_m(\mathbf{q})$  varies relatively slowly within this small segment, compared to the singularity arising in  $H_m(\mathbf{q})$ . It can therefore be assumed

constant within the segment integral. This is expressed as

$$\langle \phi_{n\mathbf{k}}^{\text{KS}} | \tilde{\Sigma}_{\text{lat}}(\omega) | \phi_{n\mathbf{k}}^{\text{KS}} \rangle = - \left( \frac{4\pi\bar{Z}}{\varepsilon_{\infty}} \right)^2 \frac{N_q}{\Omega(2\pi)^3} \sum_m \sum_i G_m(q_i) \int_{V_{\text{segment}}} d^3q'_i H_m(q'_i) \quad (6.8)$$

where  $q'_i = q_i + \tilde{q}$  and so  $G(q_i) \approx G(q'_i)$ . These segments will ultimately be modelled by the cylinders and so the final step will be to solve the integral

$$\int d\tilde{q}_{\theta} d\tilde{q}_r d\tilde{q}_z q_r \frac{1}{\left( \varepsilon_{n\mathbf{k}}^{\text{KS}} - \varepsilon_{m\mathbf{k}-\mathbf{q}}^{\text{KS}} - i\eta \right)^2 - \left( \omega_{\text{TO}}^2 + \frac{4\pi\bar{Z}^2}{\varepsilon_{\infty}\Omega_{\text{cell}}} \right)} \quad (6.9)$$

in cylindrical coordinates. In order to do this, a Taylor expansion of the energy,  $\varepsilon_{m\mathbf{k}-\mathbf{q}}^{\text{KS}}$  is made about the respective  $\mathbf{q}$ -point to the first order.

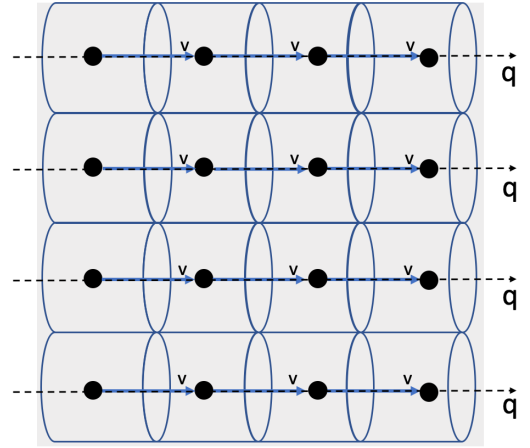
$$\varepsilon_{m\mathbf{k}-\mathbf{q}}^{\text{KS}} \approx \varepsilon_{m\mathbf{k}-\mathbf{q}}^{\text{KS}} \Big|_{\mathbf{q}=\mathbf{q}_0} + \frac{\partial \varepsilon_{m\mathbf{k}-\mathbf{q}}^{\text{KS}}}{\partial \mathbf{q}} \Big|_{\mathbf{q}=\mathbf{q}_0} \cdot \mathbf{q}, \quad (6.10)$$

which limits the integration within regions where the bands are linear. This is safe to approximate within the micro-volume segments of the Brillouin-Zone. Recognising that the group velocity  $v = \partial\varepsilon/\partial q$ , and integrating over the polar angle and radius of the cylinder results in

$$\pi q_r^2 \int_{k_0}^{q_0} dq_z \frac{1}{\left( \varepsilon_{n\mathbf{k}}^{\text{KS}} - \varepsilon_{m\mathbf{k}-\mathbf{q}_0}^{\text{KS}} - q_z v - i\eta \right)^2 - \left( \omega_{\text{TO}}^2 + \frac{4\pi\bar{Z}^2}{\varepsilon_{\infty}\Omega_{\text{cell}}} \right)} \quad (6.11)$$

where  $q_z$  denotes the change in  $\mathbf{q}$  along the cylinder of a length defined by the integral bounds (refer back to figure 6.2).

$q_{13} + \tilde{q}$ ●	$q_{14} + \tilde{q}$ ●	$q_{15} + \tilde{q}$ ●	$q_{16} + \tilde{q}$ ●
$q_9 + \tilde{q}$ ●	$q_{10} + \tilde{q}$ ●	$q_{11} + \tilde{q}$ ●	$q_{12} + \tilde{q}$ ●
$q_5 + \tilde{q}$ ●	$q_6 + \tilde{q}$ ●	$q_7 + \tilde{q}$ ●	$q_8 + \tilde{q}$ ●
$q_1 + \tilde{q}$ ●	$q_2 + \tilde{q}$ ●	$q_3 + \tilde{q}$ ●	$q_4 + \tilde{q}$ ●



(a) Segmentation of a 2D Brillouin-Zone.

(b) Cylindrical integration of a 2D Brillouin-Zone

Figure 6.3: Illustrations of the micro-volume integration solution to singularities arising in equation (5.30).

The group velocity is different for each band,  $m$ , in the sum. It is determined by evaluating the energy difference between each nearest  $\mathbf{q}$ -point. This is depicted in figure 6.3b,

again using a 2-Dimensional grid for simplicity. The integration direction is fixed in one direction and follows the group velocity of each micro-cylinder. Doing this, an attempt is made to integrate across the entire Brillouin-Zone to encapsulate all singularities. Inserting the definite solution of the integral in equation (6.11) into equation (6.8) provides the following analytic expression for the lattice correction.

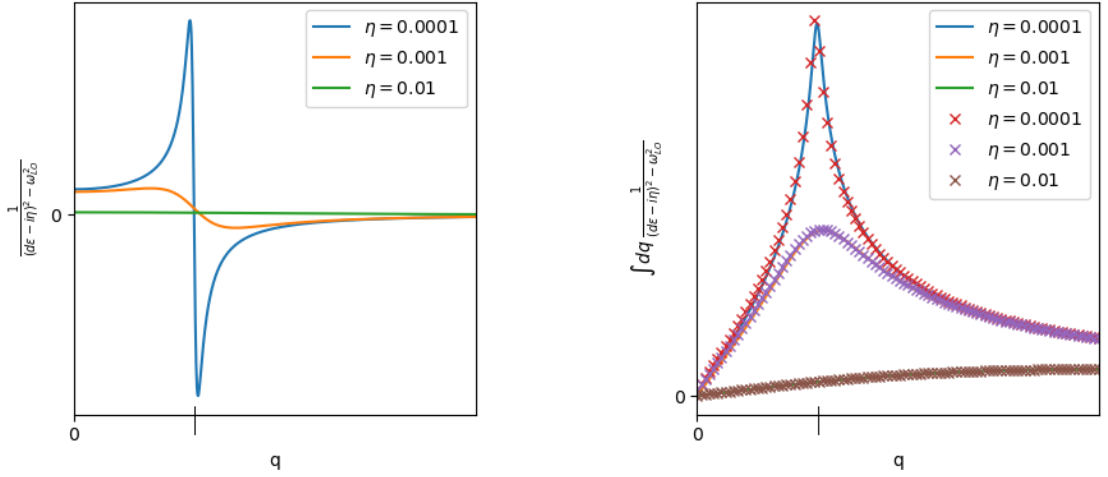
$$\begin{aligned} \langle \phi_{n\mathbf{k}}^{\text{KS}} | \tilde{\Sigma}_{\text{lat}}(\omega) | \phi_{n\mathbf{k}}^{\text{KS}} \rangle = & - \left( \frac{4\pi\bar{Z}}{\varepsilon_{\infty}} \right)^2 \frac{N_q}{\Omega(2\pi)^3} \frac{\pi q_r^2}{\omega_{\text{LO}}} \sum_m \frac{1}{v_m} \sum_{q_0} G_m(q_0) \\ & \times \left( \tanh^{-1} \left( \frac{\Delta\varepsilon_m - q_0 v_m - i\eta}{\omega_{\text{LO}}} \right) - \tanh^{-1} \left( \frac{\Delta\varepsilon_m - k_0 v_m - i\eta}{\omega_{\text{LO}}} \right) \right) \end{aligned} \quad (6.12)$$

where  $\omega_{\text{LO}}^2 = \omega_{\text{TO}}^2 + \frac{4\pi\bar{Z}^2}{\varepsilon_{\infty}\Omega_{\text{cell}}}$  as shown in equation (4.22). The radius of the cylinder is determined by the volume assigned to each  $\mathbf{q}$ -point, as shown in figure 6.3, and the length of the cylinder is set to the length to the nearest  $\mathbf{q}$ -point. The primary criteria is that the integration remains within a small region where the energy dispersion is linear, as suggested by the Taylor expansion.



6.3.2. Tuning the  $\eta$  Parameter

In equation (6.1) it is clear that the Kohn-Sham energy difference is extended by an infinitesimal quantity,  $\eta$ , which is involved in both the real and imaginary part of the expression. Analytically it is custom to evaluate the expression where  $\eta$  is allowed to vanish, however numerically a finite value must be chosen to avoid any divergence. The choice of  $\eta$  must remain a small quantity so as not to alter the behaviour of the original expression. In order to fit  $\eta$  an understanding of its effect in the given situation is required. Equation (6.12) presented an analytic solution to the cylindrical integration in  $\mathbf{q}$ -space of the lattice correction, equation (5.30), which would otherwise be solved by a numerical point-summation over the  $\mathbf{q}$ -points.



(a) Micro-volume integrand of the lattice correction exhibiting the divergence.

(b) Integration near the divergence by point-summation (cross-points) and the analytic solution, equation (6.12) (solid lines).

Figure 6.4: Behaviour for different finite  $\eta$  values, which is shown to force the divergence of the integrand to zero, and provide smoother peaks. The integration peaks at the divergence of the integrand. A dense point-summation exactly obtains the analytic result and a larger  $\eta$  requires a larger integration range.

Referring to equation (6.12),  $\eta$  is also involved in the cylindrical analytic solution. A model is constructed to present the behaviour of  $\eta$  in the present context. As described in sub-section 6.3.1, in simpler notation the integrand is

$$\frac{1}{(d\varepsilon - i\eta)^2 - \omega_{LO}^2}, \quad (6.13)$$

where  $d\varepsilon$  represents the Kohn-Sham transition energy. In this model the integration is made in a region where the energy dispersion is linear. This is fitting with the first-order Taylor expansion made in sub-section 6.3.1. From here it can be proposed that  $\eta \approx \omega_{LO}$  is too large to avoid scaling the integrand by a factor of inverse  $\eta$ . The behaviour of the integrand is present in figure 6.4a, for various finite  $\eta$  values. It is shown that introducing a finite  $\eta$  forces the divergence point to zero. Upon increasing  $\eta$  the sharp peaks become smooth curves. The integrand also switches sign around the divergence point.

To the right of this, figure 6.4b displays the definite integral from  $q = 0$  to increasing  $q$ . This is evaluated by the analytic solution in equation (6.12) represented by the solid lines

and by a point-summation represented by the cross-points. If the cross-points and solid lines coincide, this would mean that the point-summation is just as accurate as the analytic integration. With a dense number of  $\mathbf{q}$ -points, it is seen that the point-summation obtains the exact analytic result for all values of  $\eta$ . With  $\eta = 0.01$ , the integration approaches the asymptote later than for the other cases. This suggests that a larger integration range is required for larger  $\eta$  values, posing another limitation to selecting  $\eta$ , as it is only desired to perform the integral within a range where the bands are linear. A reduction of  $\mathbf{q}$ -points is presented in figure 6.5.

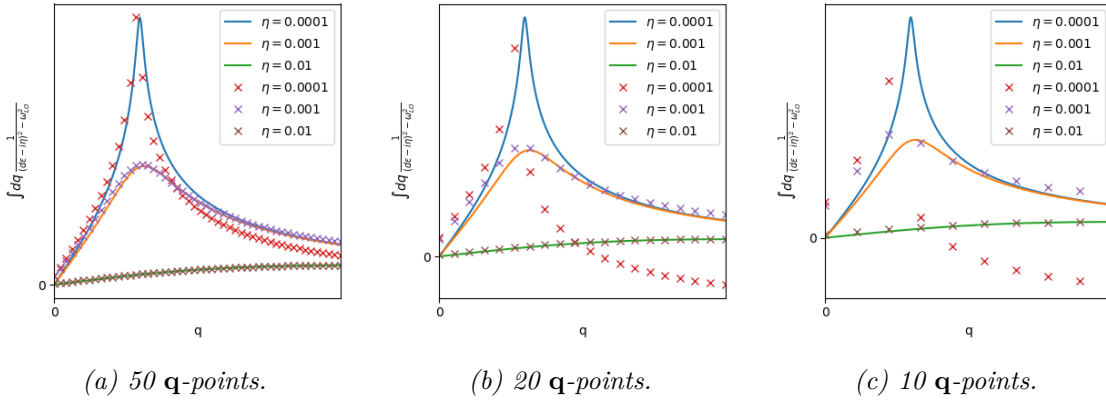


Figure 6.5: Reducing the number of  $\mathbf{q}$ -points involved in the point-summation (cross-points) against the analytic integral solution (solid line). Upon reduction, the precision deteriorates, however at a reduced rate for the higher values of  $\eta$ . Values away from the divergence point are also more precise than near the divergence.

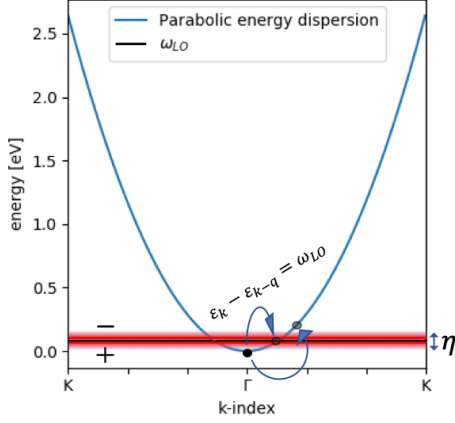
Upon reducing the  $\mathbf{q}$ -point density the point-summation solution grows less accurate. It is however particularly dependent on the value of  $\eta$ . With 10  $\mathbf{q}$ -points in this model, the integral at  $\eta = 0.01$  is exactly obtained by the point-summation, however a factor of 5 more  $\mathbf{q}$ -points is required to roughly obtain the integral at  $\eta = 0.0001$ . This implies that there is a suggested balance between the choice of  $\eta$  and the density of  $\mathbf{q}$ -points.

The sampling of the singularity on a 1-Dimensional grid is visualised in figure 6.6a. The parabolic band is fitted to the approximate energy-dispersion/band-width of Lithium-Fluoride (LiF) by an effective mass. The  $\omega_{\text{LO}}$  value also corresponds to that of LiF [10]. The lattice correction is being evaluated at the  $\Gamma$ -point in  $\mathbf{k}$ -space and the transition to two  $\mathbf{q}$ -points is highlighted. The first of these points is situated exactly at the  $\omega_{\text{LO}}$  energy line, such that a divergence occurs.

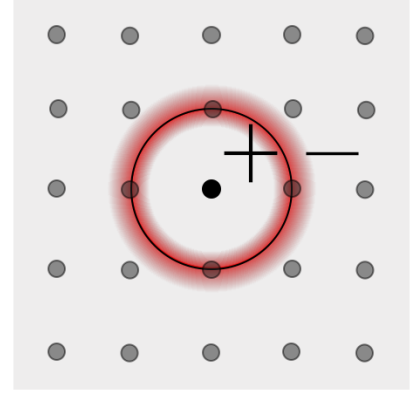
At the divergence point the integrand switches sign, as shown in figure 6.4a. The  $\omega_{\text{LO}}$  energy line thus also represents a transition region where the lattice corrections will change sign, and whether the overall correction is positive or negative depends on the positioning of this line. Here it is presented that LiF will experience an overall larger negative contribution from the integrand to the lattice corrections. The effect of  $\eta$  is illustrated by the faded red region, which represents the smoothing around the divergence point presented already in figure 6.4a. Instead of a hard line, there is now a transitional region, which allows for a proper numerical evaluation.

The same scenario is present for a 2-Dimensional grid in figure 6.6b, where a parabolic band is assumed symmetric in both in-plane directions. Where in the 1-Dimensional illustration the singularity occurred at a point, it is here shown to be a line. Extending this idea to 3-Dimensions will result in a divergence plane.

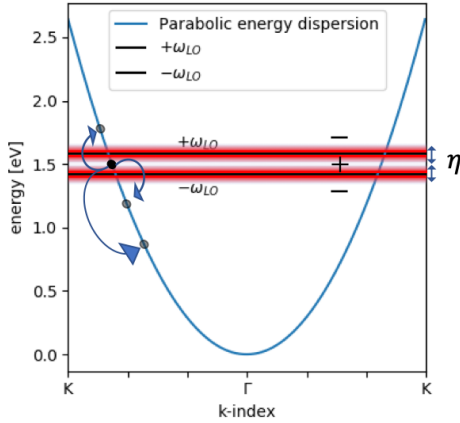
In figure 6.6c and 6.6d, the same situation is present for another, arbitrary  $\mathbf{k}$ -point where here it is shown that two divergence lines exist. Regardless, the contributions of the integrand are still predominantly negative. It is also highlighted here that with a coarse sampling density the divergence can be missed altogether. This leads to an improper treatment of the lattice correction and thus a sufficient density will be a primary factor when evaluating the corrections.



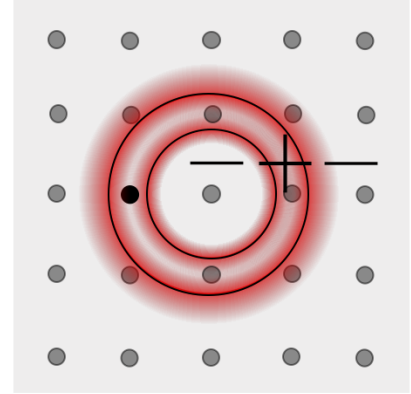
(a) 1D:  $\Gamma$ -point.



(b) 2D:  $\Gamma$ -point.



(c) 1D: arbitrary  $\mathbf{k}$ -point.



(d) 2D: arbitrary  $\mathbf{k}$ -point.

Figure 6.6: Illustrative sampling of a symmetric parabolic band in  $\mathbf{k}$ -space and the smearing effect of  $\eta$  around the divergence for LiF. The  $\omega_{LO}$  line is emphasised as a region where the sign of the integrand switches. The exact sampling on this line requires a proper sampling density and causes singularities, which  $\eta$  can assist in treating.

As long as the integration never ends at, and is always evaluated across, the divergence point, the aim is to be able to evaluate the integral to a  $\mathbf{q}$ -point past the divergence point. Figure 6.5 shows that these points are obtainable with a higher  $\eta$ , ignoring the precision at or near the divergence point. A full understanding of the behaviour would require a full 3-Dimensional integral, rather than the cylindrical integral expressed by equation (6.12). Regardless, an insight into and a framework for studying the behaviour of the integrand and its definite integral has been provided, along with the impact of  $\eta$ . It has

been shown that in the limit of linear bands,  $\eta$  can in principle be chosen arbitrarily large, as long as the integration is across a singularity. There is only a limit on the number of  $\mathbf{q}$ -points required to properly evaluate the integration. The  $\eta$  variable will remain a free variable, which will allow  $\eta$  to be increased to avoid undesired behaviour in the results from singularities.

## Correcting the Bandstructure of Lithium-Fluoride

The focus of this chapter will be on including lattice corrections to the GW bandstructure of LiF. This material is a prime candidate, as it is a highly polar material, given its significant effective Born-charge and consequently strong LO-TO phonon splitting [10]. The contents will present the construction of the primitive unit-cell along with parameters of the ground-state and GW calculation. The resulting band-structures will be displayed followed by a discussion focused on the investigation and understanding of the numerical treatment. Results based on the parameters applied in the work by Botti and Marques will be produced to extend the discussion.

### 7.1. Constructing the Primitive Unit-Cell

The primitive unit-cell of LiF is constructed using the ASE *build* module. This requires only that the atomic formula is specified, along with the crystal structure and lattice constant. The relevant parameters alongside the unit-cell are presented in table 7.1 and figure 7.1, respectively.

*Table 7.1: Parameters of the unit-cell, ground-state DFT, and GW calculations.*

Parameters	
Unit-cell [28]	
Atomic formula	LiF
Crystal structure	Rock-Salt
Lattice constant(a)	4.027 Å
Periodicity	Full
Brillouin-Zone	FCC
Ground-state [26]	
<b>k</b> -point grid	(17,17,17)
Plane-wave cut-off	800 eV
Functional	PBE
GW	
<b>k</b> -point grid	(18,18,18)
Fix density	True
Converged bands	7

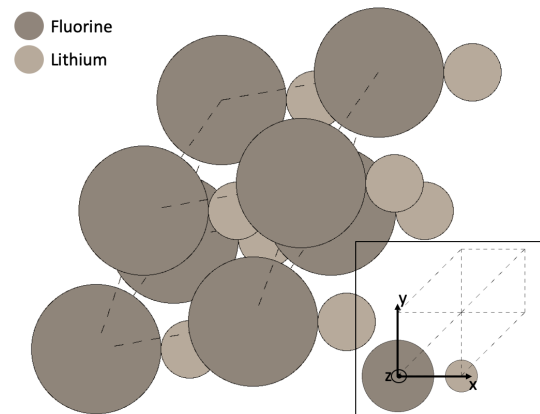


*Figure 7.1: LiF unit-cell repeated in each direction. Inset displays the bare primitive unit-cell and Cartesian directions.*

From the cell parameters of the conventional unit-cell, the lattice constant is 4.027 Å[28]. Since these parameters are based on experimental results, no relaxation has been made, as the structure is physically obtainable. The unit-cell is set to be periodic in

all directions (fully periodic). The ground-state DFT calculation is executed by the ASR Python module utilising the default parameters [26]. The  $\mathbf{k}$ -point grid is defined by a density of  $6 \text{ pts}/\text{\AA}^{-3}$ , which constructs a Monkhorst-Pack grid of (17,17,17). Along with this, the default plane-wave cut-off energy is 800 eV. These parameters are defined well above convergence values, so it is safe to assume that the  $\mathbf{k}$ -point density and plane-wave cut-off energy are well converged. The  $\mathbf{k}$ -point grid is also  $\Gamma$ -centred to ensure a sampling of the  $\Gamma$ -point. The GW calculation utilises the electron density and thus the effective potential from the ground-state calculation, known as the fixed density method. The same  $\mathbf{k}$ -point density is applied, however the number of points are set to be even in all directions constructing a Monkhorst-Pack grid of (18,18,18) that is still  $\Gamma$ -centred. The LiF Brillouin-Zone is a Face-Centred-Cubic structure, with the special path ' $\Gamma$ -X-W-K- $\Gamma$ -L-U-W-L-K|U-X' [29]. LiF consists of 4 occupied bands. 8 un-occupied bands are added, where the bands are converged up to the last 5. This results in 7 converged bands for the GW calculation.

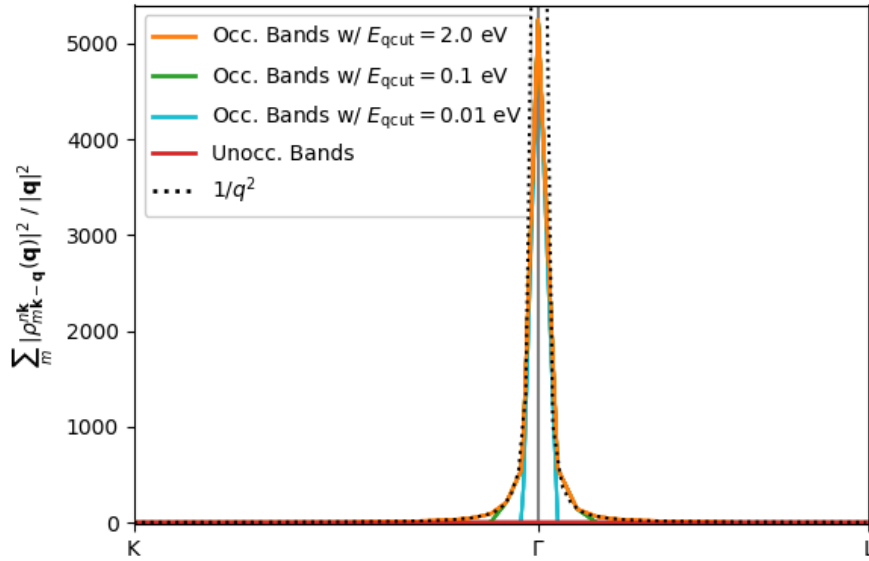
## 7.2. Convergence in $\mathbf{q}$ -space

It is of importance in this work to verify the convergence in  $\mathbf{q}$ -space. The analytic solution in equation (5.30) presents a sum over  $\mathbf{q}$ -points, in which Botti and Marques [13] argue that the  $\mathbf{q} = 0$  term provides the largest, and thus most consequential contribution. This is criticised by Lambrecht *et al.* [14] claiming that finite- $\mathbf{q}$  must be involved within a certain length scale. To treat this a mask is constructed in  $\mathbf{q}$ -space, in order to control the number of terms included in the sum over  $\mathbf{q}$ . This is defined by a cut-off energy,  $E_{q\text{cut}}$ , in eV dispersing from the  $\mathbf{q} = 0$  point. Treatment of the  $\mathbf{q}$ -limits have been highlighted successive to the derivation of the lattice correction in sub-section 5.2.1, and in the description of the implementation in section 6.2. The sum over  $\mathbf{q}$  is implemented such that the sum can be made over all  $\mathbf{q}$ -points in the Brillouin-Zone. This is however computationally demanding and in the analytic solution, equation (5.30), the  $\mathbf{q}$ -dependency is seen to converge with  $1/q^2$ . The aim is to converge the number of terms involved in the sum to catch this trend by adjusting the cut-off energy. The 'pair-density over  $\mathbf{q}$  squared' term,

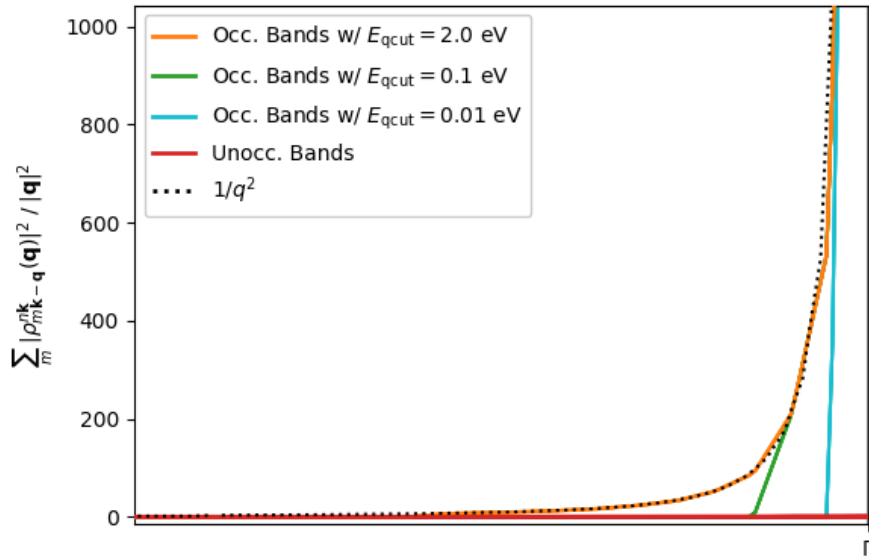
$$\sum_m \frac{|\rho_{m\mathbf{k}-\mathbf{q}}^{n\mathbf{k}}(\mathbf{q})|^2}{|\mathbf{q}|^2} \quad (7.1)$$

which is a unit-less quantity, is summed over occupied bands,  $m$ , and saved for each band,  $n$ , at the  $\Gamma$ -point in  $\mathbf{k}$ -space. Figure 7.2 presents the  $\mathbf{q}$ -dependency for all bands at three different cut-off energies, 0.01, 0.1, and 2.0 eV, along with a  $1/q^2$  line. These results are made using a  $\mathbf{k}$ -point density of  $12 \text{ pts}/\text{\AA}^{-3}$  corresponding to a Monkhorst-Pack grid of (34,34,34). Due to the size of the array in equation (7.1) memory limitations were met when attempting a higher density, which restrains the resolution of the plots.

The lines for occupied bands all over-lap, as do the lines for un-occupied bands. Immediately it is verified that the  $\mathbf{q} = 0$  point indeed carries the heaviest weight and a cut-off energy of 2.0 eV is required to capture the weight of the finite- $\mathbf{q}$  terms. Cut-off energy values lower than this force the term to vanish too early. It is also seen that all un-occupied band values are insignificant compared to the occupied band values. Referring to equation (5.30), the occupied bands contain contributions in the diagonal matrix elements (i.e.  $n = m$  terms), which represent intra-band contributions to the correction. It is therefore shown that intra-band contributions out-weigh inter-band contributions in the lattice corrections. Band-structures containing lattice corrections will be computed using a cut-off energy of 2.0 eV.



(a) Interpolated plot of values saved for expression (7.1) in  $\mathbf{q}$ -space, which presents the  $1/q^2$  behaviour. The largest contribution of  $\mathbf{q}=0$  is confirmed by the peak at the  $\Gamma$ -point.

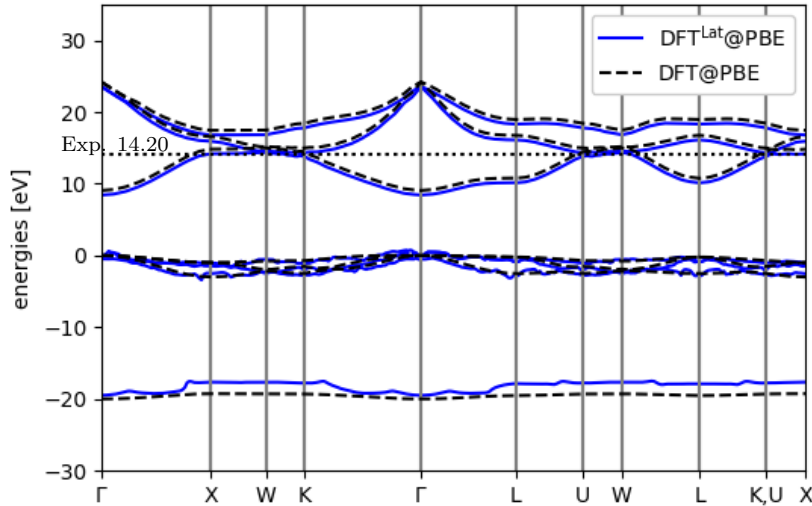


(b) Enlarged view of the above plot to emphasise the fitting of  $1/q^2$  by including more  $\mathbf{q}$ -points.  $E_{\text{qcut}} < 2.0$  eV force the function to vanish too early.

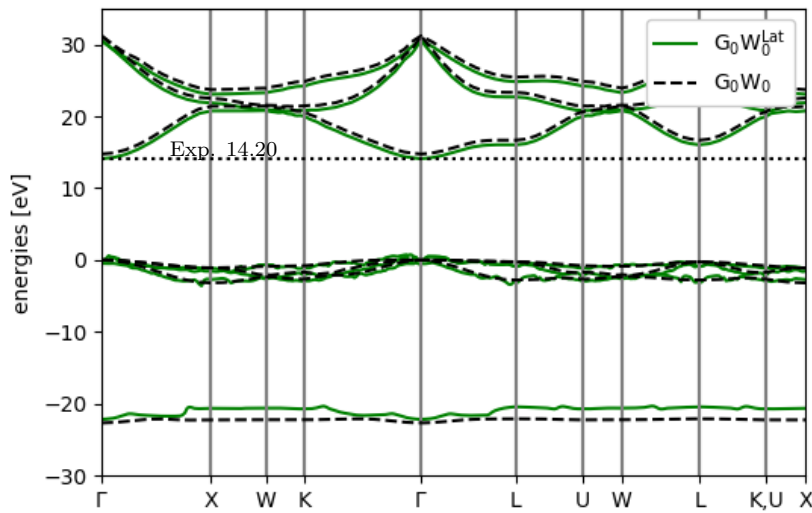
Figure 7.2: Pair-density over  $\mathbf{q}$  squared evaluated at the  $\Gamma$ -point in  $\mathbf{k}$ -space, for each band,  $n$ , and summed over occupied bands,  $m$ . The interpolated plot is in  $\mathbf{q}$ -space. The aim is to converge the number of terms involved in the sum over  $\mathbf{q}$ -points by adjusting a cut-off energy,  $E_{\text{qcut}}$ , and to catch the  $1/q^2$  trend. Occupied band values all over-lap as do all un-occupied band values, which are shown to be greatly negligible.

### 7.3. Evaluation of the Resulting Bandstructures

The lattice corrected DFT and GW band-structures are presented in figure 7.3a and 7.3b, respectively. A cut-off energy,  $E_{\text{qcut}}$ , of 2.0 eV is used and  $\eta = 0.01$ . The  $\mathbf{k}$ -point density is set to 24 pts/Å<sup>-1</sup>, which corresponds to a Monkhorst-Pack grid of (66,66,66). The valence band maximum without lattice corrections occurs at the  $\Gamma$ -point. The most valence band, both with and without lattice corrections, is set to energy zero at the  $\Gamma$ -point. This provides a constant shift to all bands. This is done primarily to provide an easy comparison to the experimental direct band-gap of 14.20 eV [30], represented by the dotted black line.



(a) DFT band-structure highlighting the under-estimation of the band-gap.



(b) GW band-structure presenting the over-estimation of the band-gap, along with the desired reduction of this over-estimation by lattice corrections.

Figure 7.3: Interpolated band-structures with and without lattice corrections. The experimental direct band-gap is represented by the black dotted line. Lattice corrections are evaluated with a Monkhorst-Pack grid of (66,66,66),  $E_{\text{qcut}} = 2.0$  eV, and  $\eta = 0.01$ . Most valence band, with and without lattice corrections, is set to 0 eV at the  $\Gamma$ -point. Lattice corrections exhibit irregularities along the BZ special path.



The under-estimation and over-estimation of the DFT and GW direct band-gap, respectively, are exhibited. The lattice corrections are shown to reduce the band-gap, which is desired for GW band-structures in order to correct their over-estimation.

It should be noted that setting the most valence band, with and without lattice corrections, to energy zero at the  $\Gamma$ -point, results in the observed negative lattice correction shift of the un-occupied bands. Without doing this, the occupied bands instead experience a positive lattice correction shift. The lattice corrections are however shown to vary sporadically. For all plots presented, if the lattice corrections were constant over the entire Brillouin-Zone special path, the lattice corrected occupied bands should all over-lap with the original occupied bands, due to the shift of the most valence bands (with and without lattice corrections) to zero energy at the  $\Gamma$ -point.

The sporadic variation of the lattice corrections to the occupied bands are attributed to the singularities discussed in section 6.3. Referring to equation (6.1), this is supported by the fact that the transition energies for the un-occupied bands will always be between two different bands so no divergences are expected, since  $n \neq m$  for all terms in the sum over occupied bands. This also means that only occupied bands experience intra-band contributions, which are shown to be the primary contributor in figure 7.2, explaining why only occupied bands are affected by the lattice corrections. Due to the irregularities of the lattice corrections, the quantitative value of the gap reduction will not be presented and in focus. After a few comments, the focus will be on investigating the variations.

It is seen that larger shifts are occurring for the lowest-lying band. Again, figure 7.2 has already shown that expression (7.1) ensures that intra-band contributions are most significant. In this far-lying band, the transition energies for inter-band transitions are larger compared to those of the closer-lying bands. The transition energies are involved in the denominator of the lattice correction and thus reduce the weight of inter-band contributions. This further promotes the significance of intra-band contributions over inter-band contributions in far-lying bands.

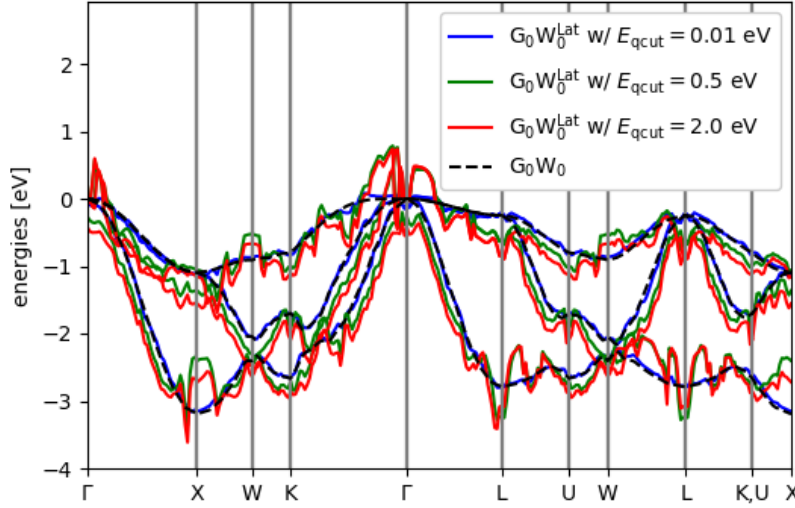
This band is also relatively flat across the entire Brillouin-Zone special path. Flat bands correspond to very localised electron states, which are more properly described in relation with local-field effects. The derivation of the lattice contribution focuses only on the head element of the dielectric matrix, which translates to only describing the macroscopic-field effects. To properly describe local-field effects, off-diagonal terms of this matrix must be included. The focus here should lie on the bands with more dispersion.

Figure 7.4a presents the close-lying occupied bands, for the GW band-structure against the lattice corrected GW band-structure, for various  $E_{qcut}$  values. The original bands are noticeably degenerate at the  $\Gamma$ -point, whereas the corrected bands are not. This suggests a required treatment of degeneracy in the evaluation. When  $E_{qcut} = 0.01$  eV, the  $\mathbf{q}$ -space mask encompasses predominantly the  $\mathbf{q} = 0$  point. For this term, in the sum of  $\mathbf{q}$ -points, the Kohn-Sham transition energy is zero, and the pair-density over  $\mathbf{q}$  squared term is constant, which results in an overall constant lattice correction. With the weight on this term, the result reveals a more constant lattice correction. Notice that the results for an  $E_{qcut}$  of 0.5 and 2.0 eV are similar, implying that the  $\mathbf{q}$ -points included beyond 0.5 eV provide only minute contributions, as also seen in figure 7.2. This suggests a possibility for a lower cut-off energy.

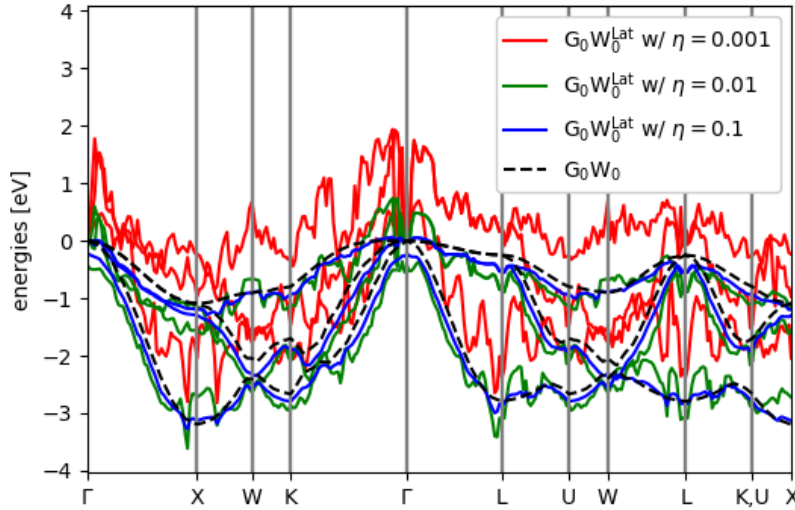
As more  $\mathbf{q}$ -points are involved in the summation, the lattice correction begins to exhibit more of these sporadic variations. The pair-densities presented in figure 7.2 did not exhibit any of this behaviour. The variations are therefore originating solely from the term involving the transition energies, and thus links to the divergences discussed in section 6.3. As more  $\mathbf{q}$ -points are included, the weight of the divergences on the overall

lattice correction increases, resulting in the presented lattice corrections.

This claim is further supported by figure 7.4b, where the bands are presented for various values of  $\eta$ . Adjusting this value was discussed in sub-section 6.3.2. Here it was shown how increasing  $\eta$  would soften the divergence peaks, and provide a more gradual transition region rather than a defined singularity point. The resulting band-structure shows how the increase of  $\eta$  directly diminishes the variations in the lattice corrections.



(a)  $E_{\text{cut}}$  dependency of the irregular variations, where it is shown that including more  $\mathbf{q}$ -points introduces sharper variations. Evaluations made using  $\eta = 0.01$ .

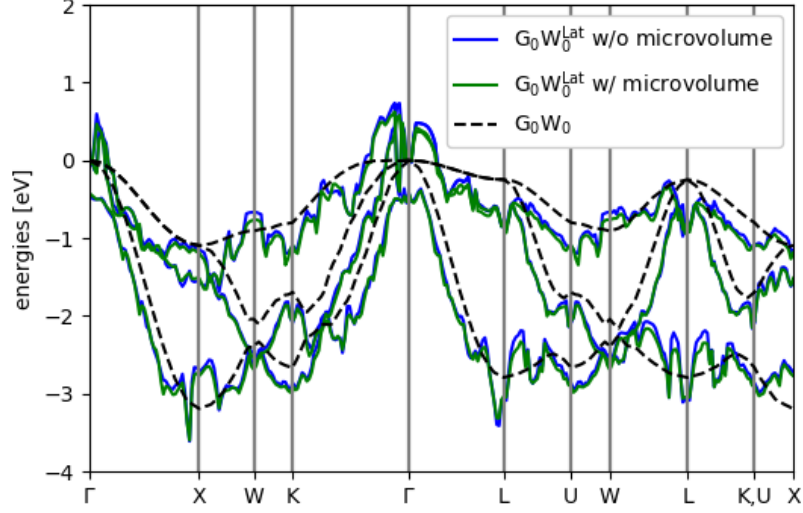


(b)  $\eta$  dependency of the irregular variations, showing that when  $\eta$  increases the variations become less prominent. Evaluations made using  $E_{\text{cut}} = 2.0$  eV.

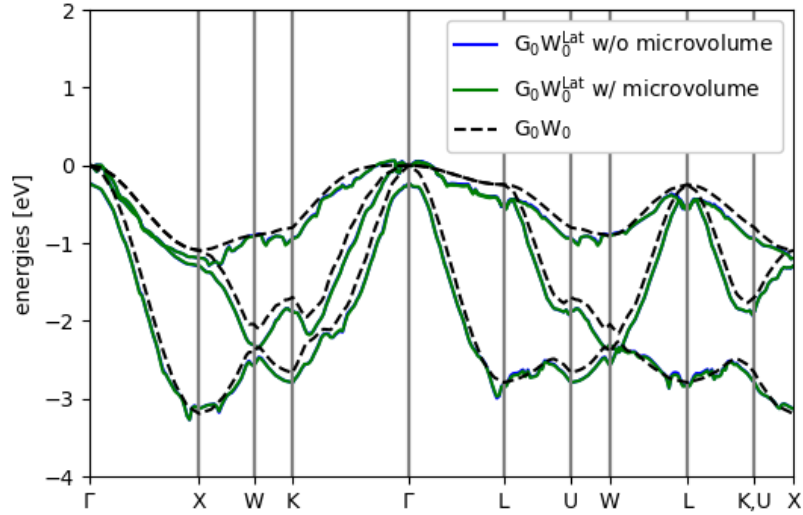
Figure 7.4: Close-lying occupied GW bands of LiF. Lattice corrections are evaluated with a Monkhorst-Pack grid of (66,66,66). Most valence band, with and without lattice corrections, is set to 0 eV at the  $\Gamma$ -point.

A solution to closing the numerical singularities was proposed in sub-section 6.3.1 by integration over micro-volumes, assigned to each  $\mathbf{q}$ -point, along a fixed direction over the entire Brillouin-Zone. Figure 7.5 compares the micro-volume integration solution to the standard solution for a  $\mathbf{k}$ -point grid of (66,66,66). The results show minute differences

when applying the micro-volume integration. The  $\eta$  parameter was adjusted from 0.01 to 0.1 and it is shown to have an equivalent affect on the micro-volume integration solution, as compared to the standard solution. This further emphasises the similarities in the result. The integration is made in one direction within the entire Brillouin-Zone. In the perpendicular directions of the integration the solution is effectively still a discrete point-summation, which is still not well-behaved as shown in the figures. This is also expected to be the reason for the similarity in the results.



(a) For  $\eta = 0.01$ , the difference between the standard solution and solution by micro-volume integration are shown to have minute differences.

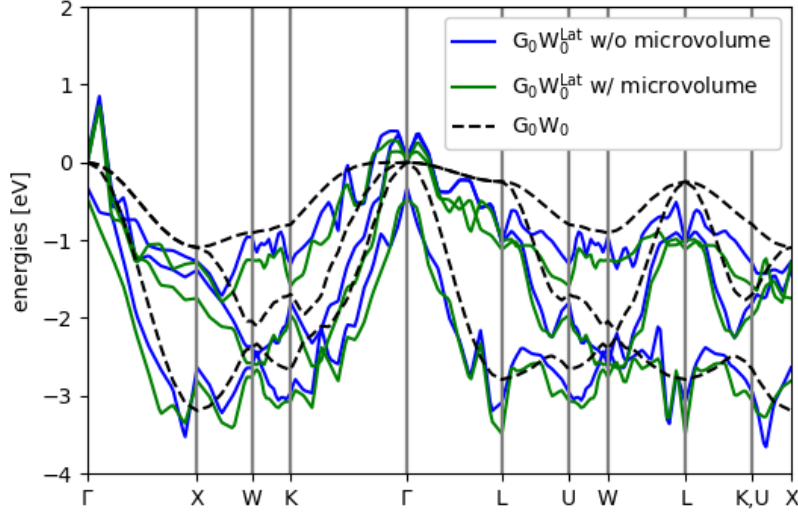


(b) For  $\eta = 0.1$ , in comparison to the plot above, this shows that  $\eta$  has the same effect on both solutions, further emphasising the strong similarity in results.

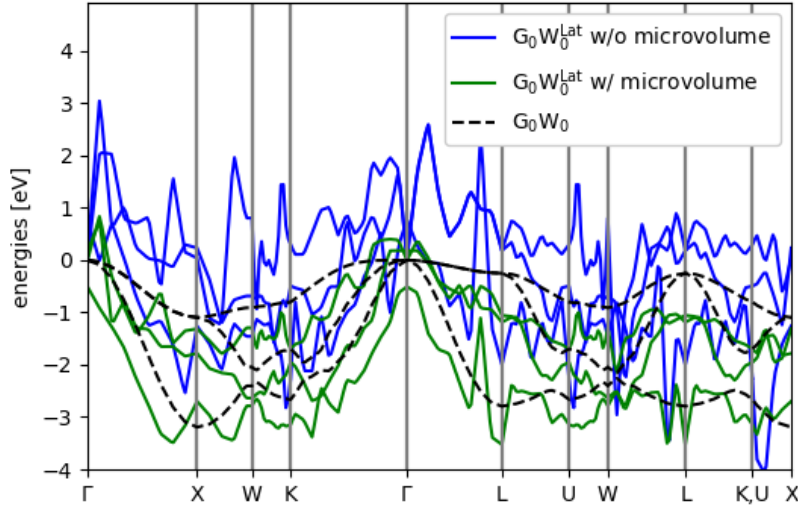
Figure 7.5: Close-lying occupied GW bands of LiF, with and without the micro-volume integration across the BZ to close singularities. Most valence band, with and without lattice corrections, is set to 0 eV at the  $\Gamma$ -point. Lattice corrections are evaluated with a Monkhorst-Pack grid of (66,66,66) and with  $E_{qcut} = 2.0$  eV.

The micro-volume integration solution is again compared to the standard solution in figure 7.6 for a less dense Monkhorst-Pack grid of (18,18,18). For  $\eta = 0.01$ , there are more noticeable differences between the micro-volume integration solution and the standard

solution. To highlight these differences, the  $\eta$  parameter is decreased to 0.001, which sharpens the peaks of divergences, as presented in section 6.3.2. This is displayed in figure 7.6b, where the standard solution exhibits tall, sharp peaks around the  $\Gamma$ -point, amongst other places. These peaks are significantly reduced by the micro-volume integration. Along the entire Brillouin-Zone special path, the micro-volume integration is shown to provide a comparatively more constant lattice correction.



(a) For  $\eta = 0.01$ , there are noticeable differences between the result from the standard solution and from the micro-volume integration.



(b) For  $\eta = 0.001$ , the difference noticed in the above plot are emphasised. Here it is shown that many of the sharp peaks in the standard solution are reduced by the micro-volume integration.

Figure 7.6: Close-lying occupied GW bands of LiF, with and without the micro-volume integration across the BZ to close singularities. Most valence band, with and without lattice corrections, is set to 0 eV at the  $\Gamma$ -point. Lattice corrections are evaluated with a Monkhorst-Pack grid of (18,18,18) and with  $E_{qcut} = 2.0$  eV.

This has highlighted the importance of the  $\mathbf{k}$ -point sampling density, in order to treat the singularity points. The  $\mathbf{k}$ -point sampling must be very high for the lattice corrections to be properly treated, as also discussed in sub-section 6.3.2. The micro-volume integration

solution is shown to reduce the extremity of the sporadic variations due to the divergences. The integration interpolates values between  $\mathbf{q}$ -points and so the necessary  $\mathbf{k}$ -point density for the integration is expected to converge faster than the point-summation. Along with this if the integration is made past a divergence point, a higher  $\eta$  is allowed, as the analytic integration is more accurate beyond the divergence point than the point-summation (figure 6.5). It is however highlighted that a 3-Dimensional implementation of the micro-volume integration is required to sufficiently treat the singularities. The  $\mathbf{k}$ -point sampling will be further discussed in the context of the work by Botti and Marques.

The results presented by Botti and Marques, motivated and inspired the implementation of lattice contributions to GW band-structures in GPAW. As described, the aim is to complete a post-processing ASR Python module for evaluating the lattice corrections. Figures 7.4 highlight that the implementation has numerical difficulties, which require special attention. This was anticipated back in the discussion of treating numerical singularities in section 6.3. Botti and Marques show that the lattice corrections are constant along the entire Brillouin-Zone special path. Their correction decreases the GW direct band-gap by  $\approx 1\text{-}2$  eV. Figure 7.7 present results utilising the parameters of Botti and Marques. They specify a  $\mathbf{k}$ -point grid of (6,6,6), which corresponds to a density of 2 pts/ $\text{\AA}^{-1}$ . This is significantly lower than the densities applied in the previous results. Along with this, only the  $\mathbf{q} = 0$  point is evaluated.

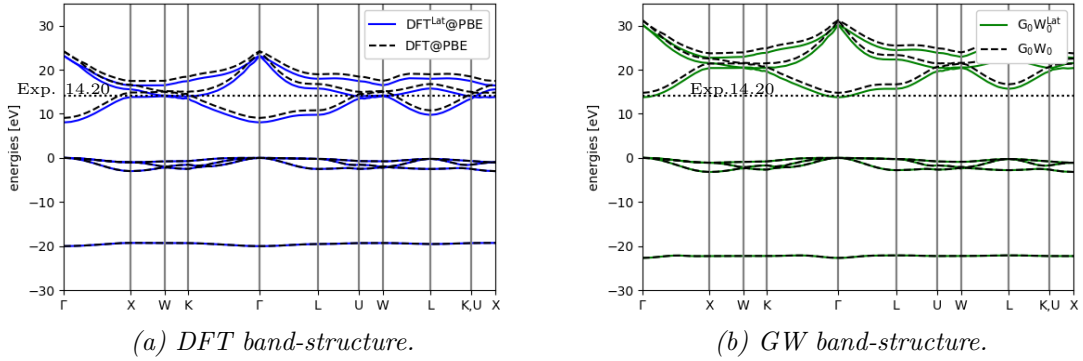


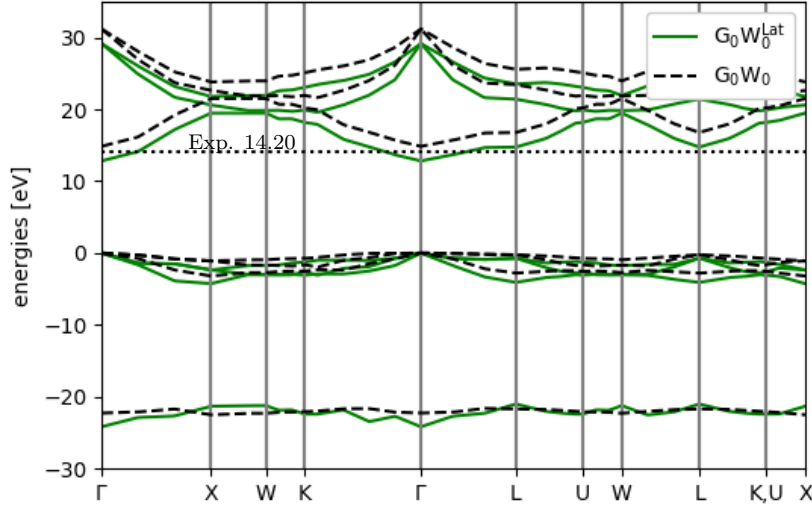
Figure 7.7: Band-structure results based on the parameters specified by Botti and Marques. The experimental direct band-gap is represented by the black dotted line. Lattice corrections are evaluated with a Monkhorst-Pack grid of (6,6,6), and only for the  $\mathbf{q} = 0$  term. No  $\eta$  value is mentioned and thus  $\eta = 0.01$  for continuity. Most valence band, with and without lattice corrections, is set to 0 eV at the  $\Gamma$ -point. Lattice corrections are shown to be constant along the entire BZ special path, as all occupied bands over-lap.

Immediately it is noticeable that no irregular variations in the lattice correction are present. The band-gap shift is not of the same order of magnitude as achieved by Botti and Marques. This result is questionable. Based on the findings in section 7.2, it can be argued that the  $\mathbf{q} = 0$  term carries the most significant contribution. Botti and Marques provide no insight into how this term is treated, however it can be assumed that the pair-density over  $\mathbf{q}$  squared term is set to a constant such that

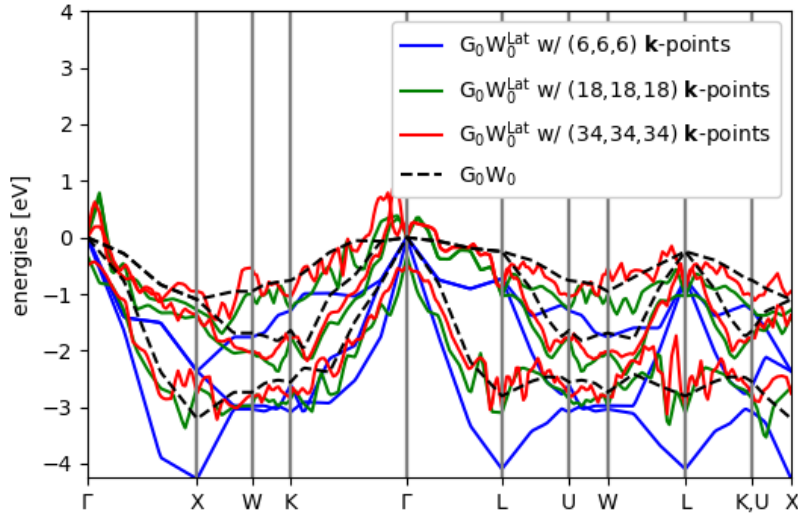
$$\lim_{\mathbf{q} \rightarrow 0} \frac{|\rho_{m\mathbf{k}-\mathbf{q}}^{n\mathbf{k}}(\mathbf{q})|^2}{|\mathbf{q}|^2} \frac{1}{\left(\varepsilon_{n\mathbf{k}}^{\text{KS}} - \varepsilon_{m\mathbf{k}-\mathbf{q}}^{\text{KS}} - i\eta\right)^2 - \omega_{\text{LO}}^2} = \text{Constant}, \quad (7.2)$$

since the Kohn-Sham transition energies will be zero. This allows for a coarse  $\mathbf{k}$ -point sampling, since no divergences occur. What the constant value is set to is unknown,

however this would define the magnitude of the correction to the band-gap. Upon including more  $\mathbf{q}$ -points, using  $E_{qcut} = 2.0$  eV and the same  $\mathbf{k}$ -point density as Botti and Marques, figure 7.8a shows that the irregular variations immediately appear. The lattice correction also increases at the  $\Gamma$ -point, since more terms are summed over.



(a) GW band-structure where lattice corrections are evaluated with a Monkhorst-Pack grid of (6,6,6) with  $E_{qcut} = 2.0$  eV, and  $\eta = 0.01$ . The experimental direct band-gap is represented by the black dotted line. Here it is shown that immediately upon including more  $\mathbf{q}$ -points, even with a coarse sampling, the irregularities in the correction appear.



(b) GW close-lying occupied bands when taking the above result and increasing the  $\mathbf{k}$ -point density, maintaining  $E_{qcut} = 2.0$  eV and  $\eta = 0.01$ . Lattice corrected bands begin to overlap the original bands as the  $\mathbf{k}$ -point density is increased, however sharper variations appear.

Figure 7.8: Results analysing the limits to the evaluation of Botti and Marques, and highlighting the importance of including finite- $\mathbf{q}$  and utilising a dense  $\mathbf{k}$ -point sampling. Most valence band, with and without lattice corrections, is set to 0 eV at the  $\Gamma$ -point.

Figure 7.8b presents an increase in the  $\mathbf{k}$ -point density. This highlights the improper evaluation of the coarse  $\mathbf{k}$ -point grid. When the density is increased, the lattice corrected occupied bands approach the original occupied bands (remember they should overlap

if the correction is constant along the entire Brillouin-Zone special path), however also capture sharper variations. It is expected that by further increasing the  $\mathbf{k}$ -point density, a convergence can be reached where the divergence is properly treated.

To finalise the discussion, the ASR Python module that has been constructed has the ability to reproduce published results. These results are, however, deemed to be oversimplified. A more careful analysis has highlighted a proper treatment in  $\mathbf{q}$ -space and the limits in the Brillouin-Zone sampling of these results. The inclusion of finite- $\mathbf{q}$  points exhibits sporadic variations in the lattice corrections, which are attributed to the presence of numerical singularities. A proper treatment of these singularities requires a highly dense  $\mathbf{k}$ -point grid. The micro-volume integration presented the ability to decrease the divergence peaks for a certain  $\mathbf{k}$ -point sampling. It is suggested that a 3-Dimensional implementation of this integration will properly treat the divergences and provide a lower convergence of the necessary  $\mathbf{k}$ -point density. The  $\eta$  parameter proved a powerful ability to flatten the variations upon increase, and it was argued that a choice of a larger  $\eta$  value is possible. Next to the 3-Dimensional micro-volume integration, solutions to further treating the singularity variations are suggested in fitting a proper  $\eta$  value along with a sufficient sampling density.





## Conclusion

The aim of this project was to implement lattice corrections to GW band-structures within GPAW, as a post-processing ASR Python module. The motivation for this was provided by Botti and Marques, showing that the inclusion of lattice contributions in the GW formalism via the dielectric function, presented band-gap corrections of  $\approx 1\text{-}2$  eV for various polar materials. The completed ASR Python module is proven successful, as it is able to produce results with the same parameters as Botti and Marques. These results are however problematic, as they do not provide a proper treatment of the evaluation in  $\mathbf{q}$ -space and sample with an arguably over-coarse  $\mathbf{k}$ -point density that mistreats numerical singularity points. These issues are focused on in the work of this project and a framework is provided to investigate the numerical issues that arise with a more detailed implementation.

The theory of this work focuses on investigating how lattice contributions can be involved in the GW framework. This starts off with deriving an expression for the lattice susceptibility, which is directly related to the dielectric function. The lattice susceptibility is shown to include the Born-charge and is assumed to contain a single dominating mode. The Born-charge is defined as the change in polarisation density divided by the displacement of a given atom in a material. It is a variable that indicates the LO-TO phonon splitting of materials and thus the long-range nature of Coulomb interactions in a system. This makes it an excellent candidate in describing the coupling between the lattice dynamics and electrostatic fields. An expression for the total dielectric function of a system is then obtained, consisting of the conventional electronic part and a corrective term arising due to the inclusion of the lattice susceptibility. To simplify the analysis, only the  $\mathbf{G} = 0, \mathbf{G}' = 0$  element of this dielectric matrix is evaluated, thus neglecting local-field effects. This term is then put to use within the screened Coulomb interaction,  $W$ , of the GW formalism. An analytic expression for the self-energy integral is solved, describing lattice contributions to the total self-energy. The frequency dependence is captured by completing a contour integration, allowing for a dynamic description of the lattice contributions. This equation closes the theoretical investigation of the inclusion of lattice dynamics in the GW formalism. A section is dedicated to the treatment of the expression in  $\mathbf{q}$ -space. The pair-density over  $\mathbf{q}$  squared is hereby evaluated in the  $\mathbf{q} \rightarrow 0$  and finite- $\mathbf{q}$  limits, where in the former it is fixed to a constant and in the latter allowed to converge as  $1/q^2$ .

Moving on to the implementation of this analytic expression as an ASR Python module, the special care of the  $\mathbf{q}$ -space treatment is highlighted. Successively, a discussion of treating numerical singularities is provided. The analytic expression is shown to diverge at several points, depending on the  $\mathbf{k}$ -point density, when the transition energies meet the LO frequency. To treat this, it is proposed to perform an integration over micro-volumes assigned to each  $\mathbf{q}$ -point. The expression for the lattice correction is solved analytically by integrating over minuscule cylindrical volumes where the band dispersion is linear.

Extending this integration in a fixed direction along the entire Brillouin-Zone should close all divergences that occur. A study of the integrand and definite integral involved in this integration was conducted, with a special focus on the infinitesimal  $\eta$  parameter and the sampling density. Analytically,  $\eta$  is allowed to vanish, however a finite value must be set when carrying a numerical evaluation. An illustration of the broadening of the singularity was provided, as increasing  $\eta$  forces the divergence point to zero and rounds off the sharp peaks. It was argued that as long as the integration is made across the divergence point,  $\eta$  should be allowed to be increased in order to avoid singularities impairing the results. A larger  $\eta$  was shown to allow for a coarser sampling density, while maintaining a proper evaluation beyond the singularity. The integration must remain within a region where the band dispersion is linear, and the required integration region to properly obtain the definite integral is shown to increase with  $\eta$ , thus posing a limit on  $\eta$ .

The resulting ASR Python module was tested on Lithium-Fluoride. An energy mask is constructed in  $\mathbf{q}$ -space, where a cut-off energy,  $E_{\text{cut}}$ , defines the number of  $\mathbf{q}$ -points involved in the evaluation. It was shown that a cut-off energy of 2.0 eV converged the result to fit the  $1/q^2$  of the pair-density over  $\mathbf{q}$  squared term, which then sufficiently includes finite- $\mathbf{q}$  points along with the  $\mathbf{q} = 0$  point. The analysis of this term also presented that inter-band contributions were insignificant compared to intra-band contributions, as the occupied bands containing intra-band contributions showed significantly larger values. The band-structures presented irregular variations in the lattice correction of the occupied bands. These variations were attributed to the singularities discussed earlier. These variations appeared upon the inclusion of finite- $\mathbf{q}$ , which explains why they do not appear when utilising Botti and Marques' parameters for the evaluation of the lattice correction. It was highlighted that a high  $\mathbf{k}$ -point density was required to properly sample the divergences. For a Monkhorst-Pack grid of (18,18,18), the micro-volume integration showed to substantially decrease many of the singularity peaks. A 3-Dimensional integration, as opposed to the integration along 1-Dimensional line segments, is suggested to be necessary for a full treatment. A lower  $\mathbf{k}$ -point density convergence is expected for the integration solution. Alongside this, increasing the  $\eta$  parameter had a strong impact as expected. At  $\eta = 0.1$ , the sporadic variations were greatly diminished. With this an insight has been provided into the numerical treatment of evaluating the lattice corrections and it is suggested that with a tuned  $\eta$  and sufficient  $\mathbf{k}$ -point sampling, a full proper implementation of the lattice corrections is obtainable. This will be aided by a 3-Dimensional micro-volume integration.

## Outlook

The initial goal of this thesis was to complete an ASR Python module to evaluate the lattice corrections and apply it on several materials. This would allow for the corrected band-gaps of several 3-Dimensional polar materials, and also an insight into the effects in 2-Dimensional materials. The field of research in 2-Dimensional materials is still in its youth and very open to new findings. The electronic screening of 2-Dimensional materials has been explored, however currently there is no investigation on the lattice screening. This would have provided a novel comparison of 2-Dimensional and 3-Dimensional materials and insight into possibly new science. This remains the long-term goal of this project.

The study of lattice polarisation effects in several materials was hindered by the great many hours of effort spent on debugging the code to understand the root of the sporadic variations present in the lattice corrections. This included an investigation of every variable involved in the evaluation, by means of analysing various plots. Amongst other things the interpolation scheme utilised for the band-structure plots was replaced in a late stage of the project, as the previous one complicated the situation. This report has gathered the primary findings from the thorough analysis and presented a framework in treating the issues. Based on the understanding achieved, it is a primary desire to be able to evaluate the lattice corrections at even greater  $\mathbf{k}$ -point densities in search of a convergence limit where all singularity peaks are well treated. This possibility is further supported by Lambrecht *et al.* [14], stating that one can choose to evaluate the static (only  $\omega = 0$ ) case, or use an ultra-fine mesh to ensure a proper integration over all divergent contributions. This was mainly limited by the computational time of evaluating the lattice correction matrix, as there is a limit to how long a calculation can run on the in-house supercomputer, Niflheim. An analysis of the time consumption throughout the code showed that the primary job is the calculation of the pair-densities. To reduce computational efforts, the pair-density calculation can be replaced with a fixed value that converges with the appropriate  $1/q^2$ . Removing the pair-density calculation and replacing it with a fixed term is expected to heavily reduce the computational load. It was also shown that inter-band contributions were insignificant and can thus be disregarded. Removing inter-band matrix elements will further reduce the calculation load. With a sufficient reduction in the computational time, an increase of the  $\mathbf{k}$ -point density will be achievable.

It was highlighted that a 3-Dimensional micro-volume integration would be required to fully treat the divergences and allow for a  $\mathbf{k}$ -point density convergence lower than that of the point-summation. To this purpose the existing method known as the tetrahedron micro-zone integration of the Brillouin-Zone is proposed. Thoroughly examined by Gilat *et al.* [31] and extended for the calculation of several spectral properties by MacDonald *et al.* [32], the tetrahedron integration method aims at accounting for the effects of variations in the matrix elements of susceptibility calculations. It provides an integration method that is applicable for various crystal structures, which would generalise the implementation for various materials beyond rock-salt crystal structures.

It was also noted in the results that original occupied bands were degenerate at the  $\Gamma$ -point, however the lattice corrected bands were not. This displays a possible issue with evaluating degenerate states. An earlier version of the code included a treatment to this by removing degenerate contributions to the sum over occupied bands. This was however removed to reduce the computational load. This may be re-introduced as an attempt to investigate and fix the issue.

The numerical treatment took a primary focus in this work, which restrained a physical investigation into the lattice contributions to the quasi-particle dressing. Two physical features highlighted here include the disregard of local-field effects and the lattice corrections occurring only for the occupied bands, which was attributed to the weighting of intra-band contributions over inter-band contributions. The latter is also observed by Bechstedt *et al.* [12] with a positive (negative) shift to the occupied (un-occupied) bands, within the COHSEX approximation. Another phenomenon highlighted by Bechstedt *et al.* is the alteration of band-widths, suggesting that the lattice correction is not constant along the entire Brillouin-Zone. This could motivate an analysis of the band-widths along with the Density-Of-States (DOS) to provide a deeper insight into the effects of the lattice contribution.

To further investigate the physical behaviour of the lattice corrections, one could construct a simple two-band model, where the band-dispersion can be parabolic or sinusoidal to ensure simplicity. This may present whether or not the lattice corrections are constant in any regions. The simple model will aid in the search of any trends or consistent behaviour of the irregular variations along with a simple tool to assist the tuning of the parameters such as  $\eta$  and the  $\mathbf{k}$ -point density, and verify the effectiveness of the micro-volume integration solution. One could tune the band-widths and compare the lattice corrections on flatter bands compared to bands with more dispersion. This could provide a picture of the lattice corrections on localised and delocalised electrons, possibly linking to the significance of local-field effects.

The inclusion of local-field effects would provide a full picture of the physical situation by allowing for an insight into the microscopic field variations and any possible coupling between these fields to the lattice dynamics. The optical phonons generate macroscopic electric fields, and therefore it is not expected that microscopic fields will have a large contribution, which is also claimed by Botti and Marques [13]. Regardless, an investigation of this would require an evaluation of the full total dielectric matrix. A simplification was presented in equation (5.8) where only the wing elements, in addition to the head element, would be required to achieve this. This could provide a more proper set of correction values for regions where the energy bands have a very low dispersion or are flat.

To further the accuracy of the physical description, the lattice susceptibility could be implemented to include more modes. A single-mode approximation was made in equation (4.21), which is valid for many relevant materials. Botti and Marques state that this is sufficient for cubic crystals with two atoms in the unit-cell. This is the case for the rock-salt crystal unit-cells. Including more infrared-active modes would generalise the evaluation to more crystal structures.

It is not believed that the COHSEX approximation would provide a more accurate quantitative evaluation of the lattice correction, however it could provide insight into qualitative behaviour. Evaluating a static case removes the divergences from the expression and presumably also the sporadic variations in the band-structure. The band-width and DOS could hereby be investigated in the COHSEX approximation with the implementation developed in this work. Along with this, the inclusion of local-field effects could be investigated in a more simple framework.





# Bibliography

- [1] Haastrup, Sten et al. “The Computational 2D Materials Database: High-Throughput Modeling and Discovery of Atomically Thin Crystals.” *2d Materials* 5.4 (2018): 042002. Web.
- [2] Calogero, Gaetano et al. “Multi-Scale Approach to First-Principles Electron Transport beyond 100 nm.” (2019): Web.
- [3] Laurent, Adèle D., and Denis Jacquemin. “TD-DFT Benchmarks: A Review.” *International Journal of Quantum Chemistry* 113.17 (2013): 2019–2039. Web.
- [4] Hai, Xiao, Jamil Tahir-Kheli, and William A. Goddard. “Accurate Band Gaps for Semiconductors from Density Functional Theory.” *Journal of Physical Chemistry Letters* 2.3 (2011): 212–217. Web.
- [5] Ferreira, Luiz G., Marcelo Marques, and Lara K. Teles. “Approximation to Density Functional Theory for the Calculation of Band Gaps of Semiconductors.” *Physical Review B - Condensed Matter and Materials Physics* 78.12 (2008): 125116. Web.
- [6] Godby, R. W., M. Schluter, and L. J. Sham. “self-energy operators and exchange correlation potentials in semiconductors.” *Physical Review B* 37.17 (1988): 10159–10175. Web.
- [7] Hüser, Falco, Thomas Olsen, and Kristian Sommer Thygesen. “Quasiparticle GW Calculations for Solids, Molecules, and Two-Dimensional Materials.” *Physical Review B* 87.23 (2013): 235132. Web.
- [8] Hybertsen, M. S., and S. G. Louie. “First-Principles Theory of Quasiparticles: Calculation of Band Gaps in Semiconductors and Insulators.” *Physical Review Letters* 55.13 (1985): 1418–21, 1418–1421. Web.
- [9] Hedin, Lars. “New Method for Calculating the One-Particle Green’s Function with Application to the Electron-Gas Problem.” *Physical Review* 139.3A (1965): A796–A822, A796–A822. Web.
- [10] Grosso, G., and G. P. Parravicini. *Solid State Physics*. Academic Press, 2000.
- [11] Shishkin, M., M. Marsman, and G. Kresse. “Accurate Quasiparticle Spectra from Self-Consistent GW Calculations with Vertex Corrections.” *Physical Review Letters* 99.24 (2007): 246403. Web.
- [12] Bechstedt, F. et al. “Quasiparticle Bands and Optical Spectra of Highly Ionic Crystals: AlN and NaCl.” *Physical Review B - Condensed Matter and Materials Physics* 72.24 (2005): 245114. Web.
- [13] Botti, Silvana, and Miguel A.L. Marques. “Strong Renormalization of the Electronic Band Gap Due to Lattice Polarization in the GW Formalism.” *Physical Review Letters* 110.22 (2013): 226404. Web.

- [14] Lambrecht, Walter R.L., Churna Bhandari, and Mark Van Schilfgaarde. “Lattice Polarization Effects on the Screened Coulomb Interaction  $W$  of the GW Approximation.” *Physical Review Materials* 1.4 (2017): 043802. Web.
- [15] Mortensen, Jens Jørgen, Lars Bruno Hansen, and Karsten Wedel Jacobsen. “Real-Space Grid Implementation of the Projector Augmented Wave Method.” *Physical Review B Condensed Matter* 71.3 (2005): 035109. Web.
- [16] Enkovaara, J. et al. “Electronic Structure Calculations with GPAW: a Real-Space Implementation of the Projector Augmented-Wave Method.” *Journal of Physics: Condensed Matter* 22.25 (2010): 253202. Web.
- [17] Kohanoff, Jorge. *Electronic Structure Calculations for Solids and Molecules: Theory and Computational Methods*. Cambridge University Press, 2006.
- [18] Ceperley, D. M., and B. J. Alder. “Ground State of the Electron Gas by a Stochastic Method.” *Physical Review Letters* 45.7 (1980): 566–569. Web.
- [19] Perdew, J. P., K. Burke, and M. Ernzerhof. “Generalized Gradient Approximation Made Simple.” *Physical Review Letters* 77.18 (1996): 3865–3868. Web.
- [20] Rieger, Martin M. et al. “GW Space-Time Method for the Self-Energy of Large Systems.” *Computer Physics Communications* 117.3 (1999): 211–228. Web.
- [21] Bruus, Henrik, and Karsten Flensberg. *Many-Body Quantum Theory in Condensed Matter Physics: an Introduction*. Oxford University Press, 2017.
- [22] Yan, Jun et al. “Linear Density Response Function in the Projector Augmented Wave Method.” *Physical Review B Condensed Matter* 83.24 (2011): 245122. Web.
- [23] Griffiths, David J. “Electric Fields in Matter.” *Introduction to Electrodynamics*. 4th ed. Cambridge: Cambridge UP, 2018. 185–86. Print.
- [24] Spaldin, Nicola A. “A Beginners Guide to the Modern Theory of Polarization.” *Journal of Solid State Chemistry* 195 (2012): 2–10. Web.
- [25] Larsen, Ask Hjorth et al. “The Atomic Simulation Environment - A Python Library for Working with Atoms.” *Journal of Physics: Condensed Matter* 29.27 (2017): 273002. Web.
- [26] Gjerding, Morten. “Atomic Simulation Recipes.” GitLab, [gitlab.com/mortengjerding/asr](https://gitlab.com/mortengjerding/asr).
- [27] Alfè, Dario. “PHON: A Program to Calculate Phonons Using the Small Displacement Method.” *Computer Physics Communications* 180.12 (2009): 2622–2633. Web.
- [28] Streltsov, V. A. et al. “Electronic and Thermal Parameters of Ions in CaF<sub>2</sub>: Regularized Least Squares Treatment.” *Soviet Physics - Crystallography* 33.1 (1988): 49–52, 49–52. Print.
- [29] Setyawan, Wahyu, and Stefano Curtarolo. “High-Throughput Electronic Band Structure Calculations: Challenges and Tools.” *Computational Materials Science* 49.2 (2010): 299–312. Web.



- [30] Piacentini, M., D. W. Lynch, and C. G. Olson. “Thermoreflectance of LiF between 12 and 30 EV.” *Physical Review B (solid State)* 13.12 (1976): 5530–43, 5530–5543. Web.
- [31] Gilat, G., and N. R. Bharatiya. “Tetrahedron Method of Zone Integration: Inclusion of Matrix Elements.” *Physical Review B (solid State)* 12.8 (1975): 3479–81, 3479–3481. Web.
- [32] Macdonald, A. H., S. H. Vosko, and P. T. Coleridge. “Extensions of The Tetrahedron Method for Evaluating Spectral Properties of Solids.” *Journal of Physics C-solid State Physics* 12.15 (1979): 2991–3002. Web.

